

# Design and Construction of a Smart Cage for Animal Handling for PET Imaging

By

Ghazaleh Mosaferchi

A Thesis submitted to the Faculty of Graduate Studies of

The University of Manitoba

in partial fulfilment of the requirements of the degree of

MASTER OF SCIENCE

Biomedical Engineering

University of Manitoba

Winnipeg, Manitoba, Canada

©2019 by Ghazaleh Mosaferchi

## **Abstract**

Positron emission tomography (PET) is a nuclear medicine imaging technique that allows quantitative evaluation of positron emitting radioactive tracers injected into a subject. In both clinical and research settings, the most commonly used radiotracer for PET imaging is the glucose analog [18F]fluorodeoxyglucose (FDG). The central strength and challenge in PET imaging is that the resulting image is of the biodistribution of the radioactively labelled tracer, rather than simply an image of anatomy. This means that biological factors can greatly influence both the appearance and quantification of the PET image, especially for FDG since it is a marker of glucose metabolism. These effective factors include fasting, anesthesia and warming the animal's body in animal PET imaging. In addition, the animals' health status must be monitored after imaging. A significant cost in routine small animal PET imaging is the labour associated with the imaging procedures. These animal centre labour costs can be reduced through use of automation and remote monitoring.

We see that there is an unmet need for a better approach to animal preparation and monitoring post-procedure and developed a 'Smart Cage'. This Smart Cage facilitates animal handling for PET imaging by using an automated food removal unit and remote monitoring of the mouse with visible light and night vision camera. We hypothesize that technology of this type can reduce variability in scan results and reduce animal technician costs associated with scanning. Consequently, we designed and constructed the hardware required for the Smart Cage and implemented an initial version of software to control and network the cage.

## **Acknowledgements**

I would like to thank my supervisor, Dr. Andrew Goertzen, for the continuous support of my M.Sc. study, for his patience, motivation and kindness. This accomplishment would not have been possible without his guidance.

I would like to thank Dr. Michel Jackson for his kind help and support during this project.

I would like to thank my friends and colleagues in the Biomedical Imaging lab at the University of Manitoba. Their support and environment of the lab have been one of the biggest influences of my academic career.

I would like to thank Ms. Judy Patterson, whose kindness and support made me feel like I am at my home country.

Most importantly, I would like to thank my husband for his endless support and continuous encouragement throughout my years of study at the UoM and through the process of researching and writing this thesis. This accomplishment would not have been possible without him.

# Table of Contents

Abstract.....	i
List of Tables .....	v
List of Figures .....	vi
List of Abbreviations .....	x
List of Copyrighted Materials.....	xi
1 Introduction and motivation.....	1
1.1 Thesis Objectives and Contributions.....	2
1.2 Thesis Organization.....	2
2 Background and context .....	4
2.1 Basic Principles of PET Imaging .....	4
2.1.1 Positron decay.....	4
2.1.2 Charged particles interaction with matter.....	5
2.1.3 Annihilation Coincidence Detection .....	6
2.1.4 PET Image Quality .....	8
2.2 Fludeoxyglucose ( $^{18}\text{F}$ ).....	9
2.2.1 Applications.....	10
2.2.2 Effect of glucose level on $^{18}\text{F}$ -FDG uptake.....	13
2.3 General procedure of $^{18}\text{F}$ -FDG PET imaging in human .....	14
2.3.1 Patient preparation.....	14
2.3.2 Essential information to performing imaging procedure.....	16
2.3.3 Radiopharmaceutical .....	17
2.3.4 PET emission imaging protocol .....	17
2.4 Impact of animal preparation on the biodistribution of $^{18}\text{F}$ -FDG.....	19
2.4.1 Dietary condition .....	19
2.5 Advantages of automated animal preparation tasks.....	23
2.6 Motion detection algorithm.....	25
2.6.1 BackgroundSubtractorMOG.....	26
2.6.2 BackgroundSubtractorMOG2.....	26
2.6.3 BackgroundSubtractorGMG.....	27
2.7 Internet of things (IoT).....	27

3	Materials and methodology .....	30
3.1	The Smart cage requirements .....	30
3.2	Hardware .....	31
3.2.1	Beaglebone Black Wireless (BBBW).....	32
3.2.2	Linear actuator .....	34
3.2.3	Logitech C930e webcam .....	36
3.2.4	Reolink C1-pro IP Camera .....	37
3.2.5	Cage's frame.....	38
3.4	Software .....	47
3.4.1	Beaglebone Black Wireless software .....	49
3.3.2	Host PC software .....	53
4.	Results .....	56
4.1	Hardware evaluation .....	56
4.1.1	Mass.....	57
4.1.2	Cost.....	57
4.1.3	Housekeeping .....	58
4.1.4	Durability.....	60
4.1.5	Potential .....	60
4.2	Software evaluation.....	61
4.3	Automating food removal .....	61
4.4	Motion tracking diagrams .....	65
5.	Conclusion and future works .....	73
5.1	Summary and conclusion.....	74
5.2	Future works .....	74
5.2.1	Capability and reproducibility test .....	75
5.2.2	Using Cloud system instead of host PC.....	75
5.2.3	Controllable heating module .....	75
5.2.4	Revising the frame of the smart cage .....	76
	References.....	77

# List of Tables

Table 2-1- Properties of common positron emitters [5]. Reprinted by permission from Copyright Clearance Center: Springer Nature, Radioactive Decay and Interaction of Radiation with Matter by Gopal B. Saha, 2016. ....	5
Table 2-2- Overview of Factors Affecting 18F-FDG PET Quantification [4]. This research was originally published in JNM. R. Boellaard, "Standards for PET Image Acquisition and Quantitative Data Analysis. J Nucl Med. vol. 50, pp. 11S - 20S, 2009.© SNMMI. ....	11
Table 2-3- 18F-FDG Radiation Dosimetry for Adults and Children [21]. This research was originally published in JNM. P. Dominique Delbeke, R. Edward Coleman, Milton J. Guiberteau, Manuel L. Brown, Henry D. Royal, Barry A. Siegel, David W. Townsend, Lincoln L. Berland, J. Anthony Parker, Karl Hubner, Michael G. Stabin, George Zubal, Marc Kachelriess, Valerie Cronin and Scot, Procedure Guideline for Tumor Imaging with 18F-FDG PET/CT 1.0. J Nucl Med. vol. 47, no. 5, pp. 885-895, 2006© SNMMI. ....	17
Table 2-4- Maximal administration volumes for rats and mice [22]. ....	18
Table 3-1- Beaglebone Black Wireless specifications [32]. ....	33
Table 3-3- Status of connected pins to the DPDT switch in linear actuator's motion control circuit. ....	35
Table 3-3- A summary of specifications of the Form 2, the printing setting for printing the models and the used material [31] ....	40
Table 4-1- Criteria defined for evaluating the hardware of the smart cage. ....	56
Table 4-2- The components' weight of the smart cage. ....	57
Table 4-3- The cost of test, evaluation, manufacture, and assembly of the smart cage's components. ....	57
Table 4-4- Mechanical properties of the Formlab clear resin [31]. ....	58
Table 4-5- Solvent compatibility of Formlab clear resin. Percent weight gain over 24 hours for a printed and post-cured 1 x 1 x 1 cm cube immersed in respective solvent [31]. ....	58
Table 4-6- Mechanical properties of ABS material [39]. ....	59
Table 4-7- Solvent compatibility of ABS material [39]. ....	59
Table 4-8- The software evaluation criteria [40]. ....	61

## List of Figures

Figure 2-1- A pair of detectors can detect a pair of annihilation photons that emitted simultaneously [1]. Reprinted from Elsevier book, Simon R. Cherry, James A. Sorenson, Michael E. Phelps, Physics in Nuclear Medicine, chapter 6, Pages 63-85, with permission from Elsevier. ....	7
Figure 2-2- (a) Creation of two back to back 511 keV annihilation photons after positron emission by the radioactive decay of fluorine-18 ( <sup>18</sup> F) (half-life, 110 min). (b) Schematic of the positron emission tomography (PET) imaging process [6]. Reused with permission of ANNUAL REVIEW OF BIOMEDICAL ENGINEERING, from J. J. Vaquero and P. Kinahan, "Positron Emission Tomography: Current Challenges and Opportunities for Technological Advances in Clinical and Preclinical Imaging Systems," vol. 17, pp. 385-414, 2017.; permission conveyed through Copyright Clearance Center, Inc. ....	7
Figure 2-3- Chemical structure of glucose and <sup>18</sup> F-FDG [11].....	10
Figure 2-4- Standardized uptake values (SUVs) of eight malignant head and neck tumors (five primary tumors and three neck metastases) in the fasting state and after oral glucose loading. This research was originally published in JNM. P. Lindholm , H. Minn, S. Leskinen-Kallio, J. Bergman , U. Ruotsalainen and H. Joensuu, Influence of the blood glucose concentration on FDG uptake in cancer--a PET study. J Nucl Med. vol. 34, pp. 1-6, 1993 © SNMMI [9].....	15
Figure 2-5- An example of PET images while the patient is fasted (left) and after glucose loading (right). The laryngeal tumor of Patient5 (arrow) is clearly visible while the patient is fasted, but after glucose loading FDG uptake in the tumor relative to that in the neck muscles is noticeably less. Consequently tumor visualization decreases. This research was originally published in JNM. P. Lindholm , H. Minn, S. Leskinen-Kallio, J. Bergman , U. Ruotsalainen and H. Joensuu, Influence of the blood glucose concentration on FDG uptake in cancer--a PET study. J Nucl Med. vol. 34, pp. 1-6, 1993 © SNMMI [9]. ....	15
Figure 2-6- Tumor FDG uptake as a function of the blood glucose level for tumors MC7-L1 and MC4-L2 [24]. Reprinted by permission from Copyright Clearance Center: Springer Nature, Molecular Imaging and Biology, A Small Animal Positron Emission Tomography Study of the Effect of Chemotherapy and Hormonal Therapy on the Uptake of 2-Deoxy-2-[F-18]fluoro-d-glucose in Murine Models of Breast Cancer, Antonio Aliaga, Jacques A. Rousseau, Jules Cadorette et al, 2007. ....	21
Figure 2-7- Examples of <sup>18</sup> F-FDG biodistribution under different states. Images show sagittal sections through mice. For anatomic reference, a contrast-enhanced microCT scan is shown. (A) Not fasted, warmed, no anesthesia. (B) Fasted, not warmed, no anesthesia. (C) Fasted, warmed, no anesthesia. (D) Fasted, warmed, no anesthesia, conscious injection. (E) Reference conditions: not fasted, not warmed, no anesthesia. (F) microCT, sagittal view for anatomic reference. (G) Not fasted, warmed, isoflurane. (H) Fasted, warmed, isoflurane. (I) Fasted, warmed, ketamine. This research was originally published in JNM. B. J. Fueger, J. Czernin, I. Hildebradt, C. Tran, B. S. Halpern, D. Stout and et al, Impact of animal handling on the results of <sup>18</sup> F-FDG PET studies in mice, J Nucl Med vol. 47, pp. 999 -1006, 2006. © SNMMI [23]. ....	22

Figure 2-8- Tumor 18F-FDG uptake under various conditions. (A) Not fasted, not warmed, no anesthesia. (B) Fasted, warmed, no anesthesia. (C) Fasted, warmed, isoflurane anesthesia. Red arrow indicates tumor; brown arrow indicates brown fat; white arrow indicates paraspinal muscle; yellow arrow indicates myocardium. This research was originally published in JNM. B. J. Fueger, J. Czernin, I. Hildebradt, C. Tran, B. S. Halpern, D. Stout and et al, Impact of animal handling on the results of 18F-FDG PET studies in mice, J Nucl Med vol. 47, pp. 999 -1006, 2006. © SNMMI [23]. ..... 22

Figure 2-9- Food deprivation prior to PET imaging. This figure shows 18F-FDG PET and CT images of two representative mice used for this comparison. In the fasted mice (A), 18F-FDG uptake in the heart, brown fat and bowels was significantly ( $p < 0.01$ ) reduced in comparison with the non-fasted animals (B). As tumor cells preferably use glucose as an energy source, tumor 18F-FDG uptake remained similar or slightly improved after fasting (C). Nevertheless, fasting of animals improved overall image contrast by significantly reducing background 18F-FDG uptake in normal tissues such as brown fat ( $p < 0.0001$ ) and bowels ( $p < 0.001$ ) (C). Modest but not statistically significant increase in kidney uptake in fasting animals was observed, indicating active removal of excess tracer from the blood pool [25]. Reprint with permission from PrekinElmer Company. .... 23

Figure 2-10- An example case of imaging study including 8 mice. It shows the essential working hours for the technician to conduct the animal preparation, imaging and follow up checkups.... 25

Figure 3-1- The functional diagram of the smart cage. .... 32

Figure 3-2- Beaglebone Black Wireless [34]..... 33

Figure 3-3- L12-P micro linear actuator with position feedback [35]..... 35

Figure 3-4- Linear actuator motion control circuit. .... 35

Figure 3-5- Logitech C930e webcam [36]..... 36

Figure 3-6- Reolink C1-pro IP camera [37]..... 38

Figure 3-7 The currently in use cage at the animal facility in the University of Manitoba..... 39

Figure 3-8- Generated 3D model of the main body of the existing cage in the animal facility at the University of Manitoba. .... 39

Figure 3-4- The 3D model of designed food container for the smart cage. It has a tilted base to make sure of food accessibility to the mouse. The food window is placed above the ground to avoid trapping the mouse tail. The rectangular hole on top of the container is for mounting the linear actuator that controls the food access window. .... 41

Figure 3-5- 3D printed food container. .... 41

Figure 3-6- The 3D model of the designed tray for mounting the essential components of the smart cage. A) The specified location for mounting the food container. B) The location of mounting the water bottle. C) The location of mounting the day camera. .... 43

Figure 3-7- The first version of designed and 3D printed model of the tray. This prototype is printed by a Formlabs Form 2 3D printer using clear resin. This model has 8mm×8mm mesh size that is too large for preventing the mouse from accessing the components on the tray. In addition, the water bottle space was not large enough to store the required water for the mouse. The thickness of the tray in this model was 1 cm which has been reduced in the next versions..... 43

Figure 3-8- Second version of designed and 3D printed model of the tray. This prototype is printed by a Formlabs Form 2 3D printer using clear resin. In this model the mesh size reduced



to 4mm×4mm. The located spot for water bottle has been changed according to the existing bottle water in the animal facility at University of Manitoba. In this design the water bottle is located on top of the tray instead of inside the cage. The camera spot is covered with a plexi glass to prevent mouse from getting outside the cage. ....	44
Figure 3-9- The 3D printed prototype of the designed tray for the smart cage. This prototype is printed with a different 3D printer, Fortus 400mc, at the OIC Precision Laboratories in one piece using ABS plastics. ....	44
Figure 3-10- The first version of designed and 3D printed model of the lid. This is the first model of the designed lid. These parts were printed in the 3D printing facility of Medical Physics department at University of Manitoba due to their large size. They are made of ABS plastics. In the first design, the water bottle was considered to be located inside the main cage’s frame. A capacitive touch screen LCD was considered to be located on the lid as user interface. ....	45
Figure 3-11- The second version of the designed and 3D printed model of the lid. In this design, the water bottle was considered to be placed on top of the tray. Consequently, the height of the lid was increased to cover the lateral load of the water bottle to prevent it from falling on other components of the smart cage. ....	46
Figure 3-12- The 3D model of the designed lid for the Smart cage. The new consideration in this design was separating the water bottle from the other components on the tray to avoid having water droplets fall on moisture sensitive components while the user puts the bottle on the tray. ....	46
Figure 3-13- The 3D printed prototype of the designed lid for the smart cage. This model was 3D printed with a Fortus 400mc 3D printer at the OIC Precision Laboratories using ABS plastics. A warpage in the lid walls were observed when it was printed with Form 2 3D printer. To avoid this warpage and being able to print the whole model in one piece, this part was built using another 3D printer. ....	47
Figure 3-19- Software diagram of the smart cage. ....	48
Figure 3-20- Network diagram of the smart cage.....	49
Figure 3-22- The virtual Florence keyboard package installed on BBBW. ....	51
Figure 3-22- Designed icon for FoodRemoval program GUI. ....	51
Figure 3-23- Designed icon for Camera module's program. ....	51
Figure 3-24- FoodRemoval module's GUI, setting today’s date and time. ....	52
Figure 3-25- Camera module's GUI.....	52
Figure 3-26- FoodRemoval module's GUI, setting desired date and time to remove food. ....	52
Figure 3-27- Camera module's GUI. Capturing images with 1 frame per minute rate for 1-hour duration. ....	52
Figure 3-28- FoodRemoval module’s GUI, Showing the remaining time to remove food from the cage. ....	52
Figure 3-29- Camera module's GUI. Recording video with 10 frames per second rate for 1-hour duration. ....	52
Figure 3-30- Host PC user interface. ....	54
Figure 4-1- a captured image from the cage area by Logitech web camera seated on the tray. This frame shows the area covered with the Logitech camera. ....	62
Figure 4-2- Captured frame from a recorded video by Logitech C930 web camera located on the tray. ....	63

Figure 4-3- Captured frame from a recorded video by Logitech C930 web camera located on the tray. As it can be seen there is a blurring on the image due to the reflective surface of PLC covering the camera spot. .... 63

Figure 4-4- A captured image using an external camera while testing the food removal unit in the animal facility at the University of Manitoba. At this moment the gate of the food container is opening. The lid has been removed while testing to have access to the camera located on the tray to change its angle..... 64

Figure 4-5- A captured image using an external camera while testing the food removal unit in the animal facility at the University of Manitoba. At this moment the gate of the food container is opening. The lid has been removed while testing to have access to the camera located on the tray to change its angle..... 64

Figure 4-6- A captured image using an external camera while testing the food removal unit in the animal facility at the University of Manitoba. At this moment the gate of the food container is closing. The lid has been removed while testing to have access to the camera located on the tray to change its angle..... 65

Figure 4-7- Motion diagram of a mouse in x direction during the night. The length of the video is 15 minutes..... 68

Figure 4-8- Motion diagram of a mouse in y direction during the night. The length of the video is 15 minutes..... 68

Figure 4-9- A captured frame of the recorded video which shows the state of animal before the detected motion. This frame was captured during the night in night vision mode. The red circle shows the area where the motion will happen. .... 69

Figure 4-10- A captured frame of the recorded video which shows the state of animal after the detected motion. This frame was captured during the night in night vision mode. The red circle shows the area where the motion happened..... 69

Figure 4-11- Motion diagram of a mouse in x direction during the day. The length of the video is 15 minutes..... 70

Figure 4-12- Motion diagram of a mouse in y direction during the day. The length of the video is 15 minutes..... 70

Figure 4-13- A captured frame of the recorded video which shows the state of animal before the detected motion..... 71

Figure 4-14- A captured frame of the recorded video which shows the state of animal after the detected motion..... 71

Figure 4-15- Motion diagram of a mouse in x and y direction during the day. The length of the video is 2 minutes. This video is recorded by Logitech C930 camera. The motion detection program ran by BBBW..... 72

Figure 4-16- Motion summary of a tested mouse during 2 hours in daylight. The recording has been started at 11:52 AM on October 18th in the animal facility at the University of Manitoba. 72

Figure 4-17- Motion summary of a tested mouse during 12 hours in daylight with 1 hour interval. The recording has been started at 11:52 AM on October 18th in the animal facility at the University of Manitoba and continued for 24 hours..... 72

## List of Abbreviations

BBBW	Beaglebone Black Wireless
ACD	Annihilation coincidence detection
PET	Positron emission Tomography
CNR	Contrast-to-noise ratio
FDG	Fluorodeoxyglucose
DPDT	Double-pole, double-throw
LOR	Line of response
IoT	Internet of things

## List of Copyrighted Materials

Figure 2-1- A pair of detectors can detect a pair of annihilation photons that emitted simultaneously. Reprinted from Elsevier book, Simon R. Cherry, James A. Sorenson, Michael E. Phelps, Physics in Nuclear Medicine, chapter 6, Pages 63-85, with permission from Elsevier [1].

Figure 2-2- (a) Creation of two back to back 511 keV annihilation photons after positron emission by the radioactive decay of fluorine-18 (<sup>18</sup>F) (half-life, 110 min). (b) Schematic of the positron emission tomography (PET) imaging process. Reused with permission of ANNUAL REVIEW OF BIOMEDICAL ENGINEERING, from J. J. Vaquero and P. Kinahan, "Positron Emission Tomography: Current Challenges and Opportunities for Technological Advances in Clinical and Preclinical Imaging Systems," vol. 17, pp. 385-414, 2017.; permission conveyed through Copyright Clearance Center, Inc[6].

Figure 2-3- Chemical structure of glucose and <sup>18</sup>F-FDG [11].

Figure 2-4- Standardized uptake values (SUVs) of eight malignant head and neck tumors (five primary tumors and three neck metastases) in the fasting state and after oral glucose loading. This research was originally published in JNM. P. Lindholm , H. Minn, S. Leskinen-Kallio, J. Bergman , U. Ruotsalainen and H. Joensuu, Influence of the blood glucose concentration on FDG uptake in cancer--a PET study. J Nucl Med. vol. 34, pp. 1-6, 1993 © SNMMI [9].

Figure 2-5- An example of PET images while the patient is fasted (left) and after glucose loading (right). The laryngeal tumor of Patient5 (arrow) is clearly visible while the patient is fasted, but after glucose loading FDG uptake in the tumor relative to that in the neck muscles is noticeably less. Consequently tumor visualization decreases. This research was originally published in JNM. P. Lindholm , H. Minn, S. Leskinen-Kallio, J. Bergman , U. Ruotsalainen and H. Joensuu, Influence of the blood glucose concentration on FDG uptake in cancer--a PET study. J Nucl Med. vol. 34, pp. 1-6, 1993 © SNMMI [9].

Figure 2-6- Tumor FDG uptake as a function of the blood glucose level for tumors MC7-L1 and MC4-L2. Reprinted by permission from Copyright Clearance Center: Springer Nature, Molecular Imaging and Biology, A Small Animal Positron Emission Tomography Study of the Effect of Chemotherapy and Hormonal Therapy on the Uptake of 2-Deoxy-2-[<sup>18</sup>F]fluoro-d-glucose in Murine Models of Breast Cancer, Antonio Aliaga, Jacques A. Rousseau, Jules Cadorette et al, 2007 [23].

Figure 2-7- Examples of <sup>18</sup>F-FDG biodistribution under different states. Images show sagittal sections through mice. For anatomic reference, a contrast-enhanced microCT scan is shown. (A) Not fasted, warmed, no anesthesia. (B) Fasted, not warmed, no anesthesia. (C) Fasted, warmed, no anesthesia. (D) Fasted, warmed, no anesthesia, conscious injection. (E) Reference conditions: not fasted, not warmed, no anesthesia. (F) microCT, sagittal view for anatomic reference. (G) Not fasted, warmed, isoflurane. (H) Fasted, warmed, isoflurane. (I) Fasted, warmed, ketamine. This research was originally published in JNM. B. J. Fueger, J. Czernin, I. Hildebradt, C. Tran, B. S. Halpern, D. Stout and et al, Impact of animal handling on the results of <sup>18</sup>F-FDG PET studies in mice, J Nucl Med vol. 47, pp. 999 -1006, 2006. © SNMMI [22].

Figure 2-8- Tumor 18F-FDG uptake under various conditions. (A) Not fasted, not warmed, no anesthesia. (B) Fasted, warmed, no anesthesia. (C) Fasted, warmed, isoflurane anesthesia. Red arrow indicates tumor; brown arrow indicates brown fat; white arrow indicates paraspinal muscle; yellow arrow indicates myocardium. This research was originally published in JNM. B. J. Fueger, J. Czernin, I. Hildebradt, C. Tran, B. S. Halpern, D. Stout and et al, Impact of animal handling on the results of 18F-FDG PET studies in mice, J Nucl Med vol. 47, pp. 999 -1006, 2006. © SNMMI [22].

Figure 2-9- Food deprivation prior to PET imaging. This figure shows 18F-FDG PET and CT images of two representative mice used for this comparison. In the fasted mice (A), 18F-FDG uptake in the heart, brown fat and bowels was significantly ( $p < 0.01$ ) reduced in comparison with the non-fasted animals (B). As tumor cells preferably use glucose as an energy source, tumor 18F-FDG uptake remained similar or slightly improved after fasting (C). Nevertheless, fasting of animals improved overall image contrast by significantly reducing background 18F-FDG uptake in normal tissues such as brown fat ( $p < 0.0001$ ) and bowels ( $p < 0.001$ ) (C). Modest but not statistically significant increase in kidney uptake in fasting animals was observed, indicating active removal of excess tracer from the blood pool [24]. Reprint with permission from PrekinElmer Company.

Table 2-1- Properties of common positron emitters. Reprinted by permission from Copyright Clearance Center: Springer Nature, Radioactive Decay and Interaction of Radiation with Matter by Gopal B. Saha, 2016 [5].

Table 2-2- Overview of Factors Affecting 18F-FDG PET Quantification. This research was originally published in JNM. R. Boellaard, "Standards for PET Image Acquisition and Quantitative Data Analysis. J Nucl Med. vol. 50, pp. 11S - 20S, 2009.© SNMMI [4].

Table 2-3- 18F-FDG Radiation Dosimetry for Adults and Children. This research was originally published in JNM. P. Dominique Delbeke, R. Edward Coleman, Milton J. Guiberteau, Manuel L. Brown, Henry D. Royal, Barry A. Siegel, David W. Townsend, Lincoln L. Berland, J. Anthony Parker, Karl Hubner, Michael G. Stabin, George Zubal, Marc Kachelriess, Valerie Cronin and Scot, Procedure Guideline for Tumor Imaging with 18F-FDG PET/CT 1.0. J Nucl Med. vol. 47, no. 5, pp. 885-895, 2006© SNMMI [21].

# Chapter 1

## 1 Introduction and motivation

One of the major methods for tomographic imaging in nuclear medicine is positron emission tomography (PET) [1] that allows quantitative evaluation of positron emitting radioactive tracers injected into a subject [2]. The ability of PET to non-invasively evaluate biochemical processes at the molecular level has made it an important research tool for studying animal models of human disease. The most commonly used radiotracer for PET imaging is the glucose analog [18F] fluorodeoxyglucose (FDG) in both clinical and research settings [3]. The main strength and challenge in PET imaging is that the image is the result of the biodistribution of the radiotracer, rather than simply an image of anatomy. This means that biological factors can greatly influence both the appearance and quantification of the PET image, especially for FDG since it is a marker of glucose metabolism. These effective factors include fasting, anesthesia and warming the animal's body in animal PET imaging [4]. In addition, the animals' health status should be monitored after imaging. A significant cost in routine small animal PET imaging is the labour associated with the imaging procedures. These animal centre labour costs can be reduced through use of automation and remote monitoring.

In view of the above facts, this thesis describes the design and construction of a smart cage that facilitates animal handling for PET imaging by automating food removal procedure and the animal remote monitoring.

## **1.1 Thesis Objectives and Contributions**

In consideration of the above points, we saw an unmet need for a better approach to animal preparation and monitoring post-procedure and developed a ‘Smart Cage’ that automates feeding and allows remote monitoring of the animal before and after the imaging. Furthermore, the requirements of follow up monitoring of animals are not unique to imaging procedures and it can be applied after surgical or other procedures. By taking advantage of an ‘internet of things’ design, treating the cage as a programmable network appliance, we are able to reduce the amount of time the animal imaging technician must spend with each subject.

The designed smart cage contains two different modules:

- Automated food removal unit
- Remote monitoring module

These modules are controlled using a control unit on the cage that is a microcomputer, the Beaglebone Black wireless. This microcomputer communicates with a host computer in a local network to send the data and receive commands from users. The user can remotely customize the cage’s setting using a GUI software interface on the host computer. In addition, the user can program the cage directly using a touch screen LCD located on the cage.

## **1.2 Thesis Organization**

This thesis has three main parts to explain the steps of the smart cage’s design and construction in detail.

In Chapter 2, an introduction to PET imaging is presented. The basic principles and the factors affecting the quality of PET imaging are reviewed briefly. In addition, <sup>18</sup>F-FDG radionuclide properties and applications are explained to demonstrate the effect of external

factors on the imaging results. Moreover, PET imaging protocols and the effect of animal preparation on the results of 18F-FDG PET imaging in small animals are reviewed to express the importance of this project.

One of the features of the smart cage is the remote monitoring module. To clarify how this module works, the common tools and algorithms for motion detection and tracking of objects using image processing are introduced in brief. Furthermore, since the smart cage is taking advantage of the internet of things technology, its concept and applications in the field of animal husbandry are reviewed in the last section of this chapter.

In Chapter 3, the design process and considerations for the smart cage are reviewed. In addition, the hardware applied to build the smart cage are described in detail. Furthermore, the software that enables users to control and customize the smart cage is explained.

In Chapter 4, the results of the smart cage's testing in the animal facility of the University of Manitoba are reviewed and discussed.

Finally, Chapter 5 presents directions for future work for improving the performance of the smart cage and extending its application.



## Chapter 2

### 2 Background and context

One of the major methods for tomographic imaging in nuclear medicine is positron emission tomography (PET). PET has gained extensive clinical acceptance and now is firmly established. In this modality, a positron emitting radiotracer is injected to the patient's body. The positron particles interact with the nearby electron in the body and annihilate. Afterward, the back to back annihilation photons are detected in the PET detectors [1].

In this section we will review the basic concepts of positron decay, its interaction with matter, the principles of PET imaging and its protocol. In addition, 18F-FDG, which is one of the most common radiotracers used in PET imaging in oncology, is briefly introduced. Then, the effect of biological factors on the 18F-FDG biodistribution is investigated.

One of the features of the smart cage is the remote monitoring module. To clarify how this module works, the common tools and algorithms for motion detection and tracking of objects using image processing are introduced in brief. Furthermore, since the smart cage is taking advantage of the internet of things technology, its concept and applications in the field of animal husbandry are reviewed in the last section.

#### 2.1 Basic Principles of PET Imaging

##### 2.1.1 Positron decay

When a radionuclide is proton rich, it decays by the emission of a positron ( $\beta^+$ ), or a positively charged electron, along with a neutrino ( $\nu$ ) which is a particle having no mass or electrical charge, Equation 2-1 [5].

$$p \rightarrow n + \beta^+ + \nu + \text{energy} \quad (2-1)$$

### 2.1.2 Charged particles interaction with matter

When energetic  $\beta^+$  particles pass through matter, they interact with the orbital electrons of the atoms in the matter and lose their energy.

The range of a charged particle is dependent on its energy, mass and charge along with the density of the matter it passes through. When the energy and charge of a particle increases, its range increases as well. In contrast, as the density and atomic mass of the matter that particles are going through it increase, the positron range decreases. Table 2-1 illustrates the range of positrons along with other properties of common positron-emitters [5].

Table 2-1- Properties of common positron emitters [5]. Reprinted by permission from Copyright Clearance Center: Springer Nature, Radioactive Decay and Interaction of Radiation with Matter by Gopal B. Saha, 2016.

<b>Radionuclide range</b>	<b>Half-life</b>	<b><math>E_{\beta^+, \max}</math> (MeV)</b>	<b>Max. <math>\beta^+</math> range (mm) in water</b>	<b>Average <math>\beta^+</math> range (mm) in water</b>
<b><math>^{11}\text{C}</math></b>	20.4 min	0.97	3.8	0.85
<b><math>^{13}\text{N}</math></b>	10 min	1.20	5.0	1.15
<b><math>^{15}\text{O}</math></b>	2 min	1.74	8.0	1.80
<b><math>^{18}\text{F}</math></b>	110 min	0.64	2.2	0.46
<b><math>^{68}\text{Ga}</math></b>	68 min	1.90	9.0	2.15
<b><math>^{82}\text{Rb}</math></b>	75 sec	3.35	15.5	4.10

As described above, when a positron passes through matter, the interaction with electrons of the absorber atoms leads to its loss of energy and it almost ceases moving. At that moment, it combines with a nearby electron, resulting in the annihilation of both particles ( $\beta^+$  and  $e^-$ ) and production of two photons of 511keV energy. These two photons are emitted in opposite directions ( $\sim 180^\circ$ ), back to back. The annihilation process is the term defining the above process. The basis of positron emission tomography (PET) is detection of the produced pair of photons in the annihilation process by two detectors [5].

### **2.1.3 Annihilation Coincidence Detection**

As described earlier, when a positron annihilates with an electron, two high energy photons are produced. These photons have identical energy and are emitted back to back, in 180-degree opposing direction, Figure 2-1. The positron usually annihilates within a few tenths of mm to a few mm of the location where it was emitted. Detection of these photons in the PET detectors occurs very close in time and allows to define their origin according to the line of response (LOR) between the two detectors that detected the photons. This process is called annihilation coincidence detection (ACD), Figure 2-2 [1].

The number of coincidences are recorded for LOR during the scan. This value shows the amount of radioactivity existing along that line during the scan. The events recorded in the LORs is binned into a projection-like data set in which groups of parallel LORs are stored together in a format called the sinogram. Typically, a sinogram stores and represents the raw data from a PET system. In this format, the parallel subsets of the lines of response represent a projection angle. A row in a sinogram represents a subset (or angle). These sinograms are the inputs to the image reconstruction process and the generated cross-sectional images are the outputs that represent the radioactivity distribution [5].



## 2.1.4 PET Image Quality

As described in “Positron Emission Tomography” by Cherry, Simon R.; Sorenson, James A.; Phelps, Michael E., evaluation of the image quality is performed by investigating its measured or calculated physical characteristics. These characteristics include:

- 1) Spatial resolution (detail or sharpness)
- 2) Contrast (difference in image density or intensity between areas of the imaged object containing different concentrations of radioactivity)
- 3) Noise (statistical noise caused by random fluctuations in radioactive decay, or structured noise, e.g., resulting from instrument artifacts). These factors are not totally independent and variation in one aspect will affect the others [7].

Different levels of radionuclide uptake in the patient’s body results in an image with nonuniform intensity. This concept is known as image contrast. In nuclear medicine imaging, image contrast is mainly dependent on properties of the radionuclide. In general, using a radionuclide with highest lesion-to-background uptake or concentration ratio is desirable. In nuclear medicine imaging, factors which affect the image contrast also have impacts on the statistical noise level, specifically contrast-to-noise ratio (CNR), in the image [7].

Generally, contrast is the ratio of signal change in a desired area, such as a lesion, relative to the signal level in surrounding parts of the image. The contrast of the lesion is defined as:

$$C_l = \frac{R_l - R_o}{R_o} = \frac{\Delta R_l}{R_o} \quad (2-2)$$

Where  $\Delta R_l$  is the change in counting rate over the lesion relative to the surrounding background and  $R_o$  is the counting rate over normal tissue and  $R_l$  is the counting rate over a

lesion. Contrast sometimes is expressed as a percentage. It is possible that the image contrast is mainly affected by additional background counting rates that are applied uniformly over the activity distribution of interest. The loss of contrast can degrade visibility of low-contrast objects and subtle details in the image [7].

## 2.2 Fludeoxyglucose ( $^{18}\text{F}$ )

Fludeoxyglucose F18, or 18F-FDG, is a radiotracer used in PET imaging. Chemically, it is 2-deoxy-2- $(^{18}\text{F})$  fluoro-D-glucose, a glucose analog, in which the hydroxyl group at the C-2 position of glucose is substitute with the positron emitting radionuclide fluorine-18, Figure 2-3.

18F-FDG is a radiotracer for evaluating the metabolism of the tissue or organ since its uptake by the tissue is a marker for glucose uptake [8]. It is preferentially taken up by cells which use high levels of glucose, including brain, brown fat, kidney and cancer cells [9].

Once glucose is transported into the cell, it is trapped in it due to phosphorylation. At that time, it follows the remaining steps of glycolysis. However, the missing hydroxyl group in 18F-FDG prevents the progression of glycolysis. The 18F-FDG-6-phosphate which is formed after phosphorylation is trapped in the cell and decays radioactively. Therefore, the distribution of 18F-FDG is a good marker for glucose uptake and phosphorylation by the cells in the body.

Glucose-6-phosphate and heavy oxygen ( $^{18}\text{O}$ , or oxygen with 10 neutrons) in the hydroxyl at the C-2 position are the remaining products after 18F-FDG decaying. The glycolysis process can proceed now. Theoretically, all 18F-FDG radioactively eliminates with half-life of 110 minutes. However, clinical studies have shown that approximately 25% of FDG is cleared by the renal

system with a biological half-life of 16 minutes. For this reason, the renal-collecting system and bladder are prominent in a normal PET scan [10].

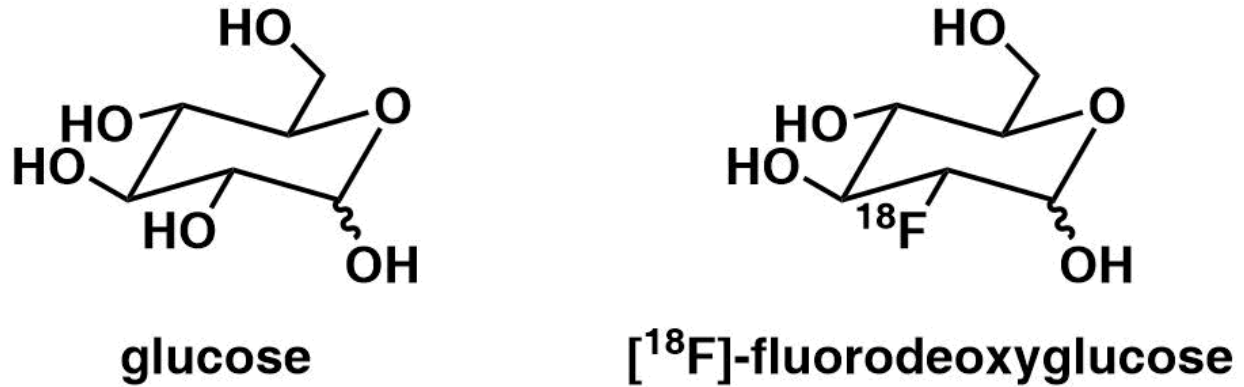


Figure 2-3- Chemical structure of glucose and <sup>18</sup>F-FDG [11].

### 2.2.1 Applications

<sup>18</sup>F-FDG is used for the evaluation of many types of cancer, including tumor diagnosis, staging, restaging, treatment monitoring, and radiation therapy planning in PET imaging [12]. It can also be used for assessment of glucose metabolism in different organs including brain, lungs and heart.

The common and simplified way to assess the PET imaging using <sup>18</sup>F-FDG radiotracer is analyzing its uptake in terms of Standardized Uptake Value (SUV). The SUV illustrates the <sup>18</sup>F-FDG tumor uptake, measured over a certain time interval after <sup>18</sup>F-FDG administration and normalized to the injected dose of <sup>18</sup>F-FDG and to a factor (such as body weight) that takes into account distribution throughout the body. SUV is calculated using the following equation [13].

$$SUV = \frac{r}{(a'/w)} \quad (2-3)$$

where  $r$  is the radioactivity activity concentration [kBq/ml] measured by the PET scanner within a region of interest (ROI),  $a'$  is the decay-corrected amount of injected radiolabeled FDG [kBq], and  $w$  is the weight of the patient [g], which is used as a substitute for a distribution volume of tracer [13].

Several physiologic and technical factors affect the SUV. Each of these factors affects the calculated SUV value and makes it unreliable to be applied in other sites and multicenter studies. To address this issue, different methods and standards are provided to minimize the effect of biological and technical factors on SUV. Table 2-2 shows an overview of the factors affecting SUV [4].

Table 2-2- Overview of Factors Affecting 18F-FDG PET Quantification [4]. This research was originally published in JNM. R. Boellaard, "Standards for PET Image Acquisition and Quantitative Data Analysis. J Nucl Med. vol. 50, pp. 11S - 20S, 2009.© SNMMI.

Category	Factor	Explanation	Typical range (maximum effect)*
Technical errors	Relative calibration between PET scanner and dose calibrator	Systematic error in SUV is equal to error in relative calibration between PET scanner and dose calibrator	-10%-10% ( $\pm 50\%$ )
	Residual activity in syringe or administration system	Lower net administered dose results in incorrect lower uptake level and SUV	0%-5% (typically <15%, but can be much greater in worst-case situations)
	Incorrect synchronization of clocks of PET/CT camera and dose calibrator	Incorrect decay correction results in incorrect SUV	0%-10% (21%, as seen in ongoing multicenter study)
	Injection vs. calibration time	Incorrect time interval is used for decay correction of administered dose	0%-10%
	Paravenous administration of 18F-FDG	Rate and quantity of delivery of 18F-FDG to tumor are reduced, resulting in incorrect SUV	0%-50% or more, strongly depending on quality of administration
Biologic factors	Blood glucose level	Lower uptake levels or SUVs occur with increasing blood	-15%+15% ( $\pm 75\%$ )



		glucose levels	
	Uptake period	Higher SUVs occur at increasing time intervals between injection and start of PET study	10%--15% at 60–90 min ( $\pm 30\%$ )
	Patient motion or breathing	Image artifacts result from mismatches in positions between CT-AC and PET emission scans, and lower SUV may result from respiratory motion (resolution loss)	0%-30% ( $\pm 60\%$ )
	Patient comfort	Patient stress and poor waiting conditions result in uptake of 18F-FDG in muscle or brown fat and affect SUV quantification	mainly giving rise to false-positive results (SUVBW 5 2–12) and possibly incorrect SUV in case of spillover
	Inflammation	Inflammatory processes near or at tumor result in false-positive increase in SUV	mainly giving rise to false-positive results and possibly incorrect SUV in case of spillover
Physical factors	Scan acquisition parameters	SNR of PET scan is affected, e.g., lower SNR results in upward bias of SUV	0%-15% ( $\pm 15\%$ )
	Image reconstruction parameters	Insufficient convergence and lower resolution result in lower SUV and increase in partial-volume effects; insufficient convergence makes SUV more dependent on surrounding activity distributions	-30%-0% (-30%)
	ROI	SUV outcome is strongly dependent on size and type of ROI used	0%-55% ( $\pm 55\%$ )
	Normalization factor for SUV	SUV outcomes are numerically different when body weight, body surface area, and lean body mass are used as normalization factors in SUV equation	Trivial
	Blood glucose level correction	Higher serum glucose level results in underestimation of SUV; use of serum glucose level correction in SUV equation therefore results in different SUV outcomes	-15%-15% ( $\pm 75\%$ )
	Use of contrast agents during CT-AC	Overestimation of attenuation and therefore higher SUV (upward bias) may occur	0%+15% ( $\pm 50\%$ )

As Table 2-2 shows, blood glucose level can have a significant effect as large as 75% on SUV. It comes from the fact that 18F-FDG uptake in tumors can be significantly affected by

blood glucose levels. It is the result of 18F-FDG and glucose competition for glucose transport and phosphorylation [14]. As a result, there is a correlation between plasma glucose levels, serum insulin levels, and the biodistribution of 18F-FDG. 18F-FDG uptake decreases as glucose levels increase in the brain and tumors because due to the mentioned competition between them [15].

### **2.2.2 Effect of glucose level on 18F-FDG uptake**

As mentioned in previous section, glucose and 18-FDG compete for glucose transport and phosphorylation. Many studies have investigated the effect of glycemia on the 18F-FDG uptake in different organs and tissues. Busing et. al [16], Keramida et. al [17], Vigilanti et. al [18], and Claeys et. al [19] reported a significant impact of the glucose level on the 18F-FDG uptake in brain. They showed that the  $SUV_{max/min}$  is higher in patients with lower glycemia than in those with higher glycemia. Furthermore, the correlation between SUV and the blood glucose levels remained noticeable after considering and applying possibly affecting factors, such as body mass index (BMI), time delay from injection to imaging, and diabetes mellitus (DM) [20]. In addition, in vitro studies show that 18F-FDG concentration in cancer cells decreases as the blood glucose level increases. As a result, fasting for a minimum of 6 hours before 18F-FDG injection should be considered to decrease the glycemia and increase radiotracer uptake [9].

As a conclusion of the above facts, the standardization of quantitative 18F-FDG PET studies is required and can be reached by the standardization of different principles. One of the most important and easier to conduct standardization procedure is the patient preparation procedure. The patient preparation procedures affect 18F-FDG uptake in both healthy tissues and tumors. These procedures are performed to maximize tumor uptake and minimize healthy tissue uptake, and consequently optimize image quality and reduce SUV variability among subjects. Several

studies offered different guidelines for patient preparation. However, the mutual considerations between different procedures include a fasting period to reach euglycemic conditions, hydration, use of sedatives and waiting conditions, bladder voiding or use of diuretics, and limits for blood glucose levels. Also, it is necessary to measure the weight and the height of the patient at the time of each PET study for SUV normalization procedure. In addition, the total administered dose stated at the dose calibration time or injection time, must be exactly known since they will be used to calculate the SUV [4].

## **2.3 General procedure of $^{18}\text{F}$ -FDG PET imaging in human**

### **2.3.1 Patient preparation**

The optimum patient preparation procedure for PET/CT is progressing. The main objectives of this procedure is minimizing radiotracer uptake in normal tissues, such as the myocardium and skeletal muscle, while maximizing uptake in target tissues such as tumors. The following protocol is a commonly used one [21].

#### 1. Before arrival

Patients should be fasted for at least 4–6 h before the administration of  $^{18}\text{F}$ -FDG to decrease physiologic glucose levels and to reduce serum insulin levels to near basal levels. Moreover, they should avoid consuming beverages other than water. Oral hydration with water is beneficial. Intravenous fluids containing dextrose or parenteral feedings also should be on hold for 4–6 h [21]. **Error! Reference source not found.** and Figure 2-5 show the importance of fasting in the visibility of tumors and SUV level in PET imaging.

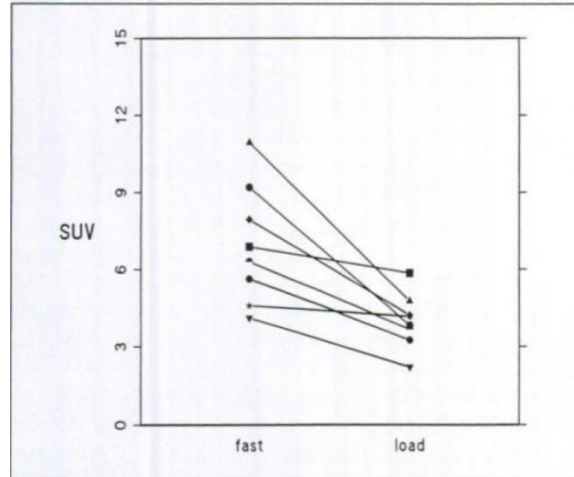


Figure 2-4- Standardized uptake values (SUVs) of eight malignant head and neck tumors (five primary tumors and three neck metastases) in the fasting state and after oral glucose loading. This research was originally published in JNM. P. Lindholm , H. Minn, S. Leskinen-Kallio, J. Bergman , U. Ruotsalainen and H. Joensuu, Influence of the blood glucose concentration on FDG uptake in cancer--a PET study. J Nucl Med. vol. 34, pp. 1-6, 1993 © SNMMI [9].

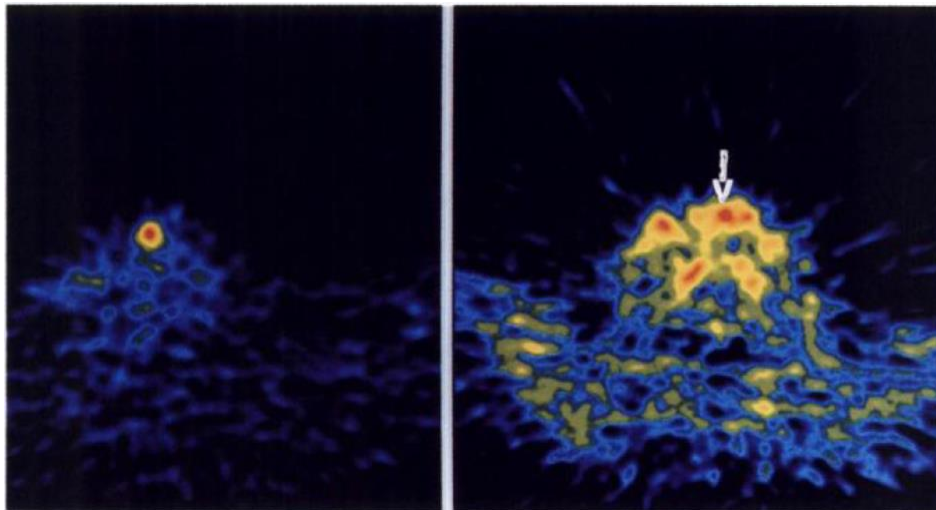


Figure 2-5- An example of PET images while the patient is fasted (left) and after glucose loading (right). The laryngeal tumor of Patient5 (arrow) is clearly visible while the patient is fasted, but after glucose loading FDG uptake in the tumor relative to that in the neck muscles is noticeably less. Consequently tumor visualization decreases. This research was originally published in JNM. P. Lindholm , H. Minn, S. Leskinen-Kallio, J. Bergman , U. Ruotsalainen and H. Joensuu, Influence of the blood glucose concentration on FDG uptake in cancer--a PET study. J Nucl Med. vol. 34, pp. 1-6, 1993 © SNMMI [9].

## 2. Before injection

a. For brain imaging, during 18F-FDG administration and the subsequent uptake phase, the patient should be in a quiet and dimly lit room [21].

b. For body imaging, to prevent muscular uptake, the patient should stay seated or lie for 18F-FDG administration and the following uptake period [21].

c. Before 18F-FDG administration, the blood glucose level should be measured and checked. Hyperglycemia reduces 18F-FDG tumor uptake. The PET scan should be cancelled if the blood glucose level is greater than 150–200 mg/dL. Insulin can be administered to reduce the serum glucose level, but there should be a delay before the administration of 18F-FDG following insulin administration. The duration of the delay depends on the type and route of administration of insulin [21].

### **2.3.2 Essential information to performing imaging procedure**

The following information must be recorded before performing imaging procedure according to “Procedure Guideline for Tumor Imaging with 18F-FDG PET/CT 1.0” published in Journal of Nuclear Medicine in 2006 [21].

1. Focused history, including the type and site of tumor, dates of diagnosis and treatment (biopsy results, surgery, radiation, chemotherapy, and administration of bone marrow stimulants and steroids), and current medications [21].

2. History of diabetes, fasting state, and recent infection [21]

3. Patient’s ability to lie still for the duration of the acquisition (15–45 min) [21]

4. History of claustrophobia [21]

5. Patient’s ability to put his or her arms overhead [21]

### 2.3.3 Radiopharmaceutical

Table 2-3 shows the radiation dose to the patient from the radiation dose for the PET radiopharmaceutical study.

Table 2-3- 18F-FDG Radiation Dosimetry for Adults and Children [21]. This research was originally published in JNM. P. Dominique Delbeke, R. Edward Coleman, Milton J. Guiberteau, Manuel L. Brown, Henry D. Royal, Barry A. Siegel, David W. Townsend, Lincoln L. Berland, J. Anthony Parker, Karl Hubner, Michael G. Stabin, George Zubal, Marc Kachelriess, Valerie Cronin and Scot, Procedure Guideline for Tumor Imaging with 18F-FDG PET/CT 1.0. J Nucl Med. vol. 47, no. 5, pp. 885-895, 2006© SNMMI.

Patient	Intravenously administered activity	Organ receiving the largest radiation dose, mGy/MBq (rads/mCi)	Effective dose, mSv/MBq (rems/mCi)
Adult	370–740 MBq, (10–20) mCi	Bladder, 0.16 (0.59)	0.019 (0.070)
Child (5 y old)	5.18–7.4 MBq/kg (0.14–0.20) (mCi/kg)	Bladder 0.32 (1.2)	0.050 (0.18)

### 2.3.4 PET emission imaging protocol

The radiotracers should be injected at a site contralateral to the region of interest. Passing at least 45 min after radiopharmaceutical injection, imaging can be done. The optimal 18F-FDG distribution phase is debatable. Many facilities begin imaging at 60 or 90 min after 18F-FDG administration. Some facilities acquire a second set of images to evaluate the variance in 18F-FDG uptake over time [21].

The duration of imaging depends on the administered activity, patient body weight, and the PET scanner sensitivity. It varies from 2 to 5 min or longer per bed position for body imaging. Typically, for imaging skull to midhigh, the total acquisition time ranges from 15 to 45 min. The imaging duration normally is longer than usual for imaging the brain or for images of a limited region of interest [21].

As described above, there are several considerations for patient preparation for 18F-FDG PET imaging in human. However, these preparations are not only for human. Although there is not a thorough standard protocol for animal preparation for 18F-FDG PET imaging, there are some important factors that must be considered before imaging the animals. In 18F-FDG PET imaging, due to the effect of plasma glucose level on the radiotracer uptake in different organs, the animal must be fasted for a period of time before imaging. Generally, after 7 hours of food deprivation the mice reach to the level of torpor. It should be noted that the fasting period should be kept minimum. In addition, since the rodents feed during the night mostly, it is better to avoid the fasting the rodents during the night. Furthermore, similar to human preparation, water should not be withdrawn from animals [22].

Another important factor in animal preparation for 18F-FDG PET imaging is the radiotracer dosage. In mice, due to small volume of their blood, a limited volume of tracer can be applied. According to the NC3Rs guidelines, Table 2-4- Maximal administration volumes for rats and mice shows recommended (maximal) volumes applied by various routes for mice and rats according to the NC3Rs guidelines. [22]

Table 2-4- Maximal administration volumes for rats and mice [22].

<b>Route</b>	<b>Rat</b>	<b>Mouse</b>
<b>Intravenous bolus</b>	5 mL/kg (1 mL/200 g rat)	10 mL/kg (0.2 mL/20 g mouse)
<b>Intraperitoneal</b>	10 mL/kg (2 mL/200 g rat)	20 mL/kg (0.4 mL/20 g mouse)
<b>Oral</b>	20 mL/kg (4 mL/200 g rat)	20 mL/kg (0.4 mL/20 g mouse)
<b>Subcutaneous</b>	10 mL/kg (2 mL/200 g rat)	20 mL/kg (0.4 mL/20 g mouse)

## **2.4 Impact of animal preparation on the biodistribution of 18F-FDG**

The usefulness of small animal PET imaging to investigate animal models of human disease and effect of the potential therapies has been proven over the years. Many research groups focus on improving image quality by developing new hardware and software. Other factors that affect the result of PET imaging are physiological parameters of the animals including dietary condition, ambient temperature and mode of anesthesia. There are a few groups who have conducted studies focusing on the effects of these factors. They have shown the physiological parameters of the animal affect the biodistribution of the radiotracer in its body and consequently the results. In the following section, we will briefly review the methodology of their experiments and the results.

### **2.4.1 Dietary condition**

The effect of fasting on 18F-FDG biodistribution from human PET studies is already known. Similarly, other research groups evaluated regional 18F-FDG uptake in rats by tissue sampling. Fueger et al [23], systematically studied effects of physiological parameters on biodistribution of 18F-FDG in mice. To evaluate the effect of dietary condition they imaged 6 mice with 10-12 weeks of age under reference (no fasting, no warming) and fasting condition. In fasting condition, the mouse did not eat food for 8 to 12 hours before the injection. Regions of interest were brain, brown adipose tissue, heart, liver, paraspinal muscle, kidney, Harderian glands, and subcutaneous tumors. Under the reference condition (no warming and no fasting, Figure 2-7 E), the highest 18F-FDG uptake was seen in brown fat (SUV,  $4.9 \pm 1.1$ ), Harderian glands (SUV,  $2.2 \pm 0.5$ ), skeletal muscle (SUV,  $2.0 \pm 0.26$ ), and myocardium (SUV,  $1.7 \pm 0.5$ ). Fasting reduced 18F-FDG uptake of skeletal muscle by 31% ( $P = 0.001$ ) and of brown fat by 32% ( $P =$



0.006). In addition, they evaluated the tumor to organ ratio uptake after imaging groups of 3 (A431) and 6 (U251) tumor bearing mice under combined fasting and warming condition. Since 18F-FDG is a glucose analog, tumor 18F-FDG uptake decreases with increasing blood glucose levels. Additionally, 18F-FDG uptake by skeletal muscles and myocardium is increased by insulin although it has no effect on 18F-FDG uptake of cancer cells. Therefore, tumor 18F-FDG uptake and image contrast are lower in the nonfasted state (high insulin and glucose levels) than in the fasted state (low insulin and glucose levels). Lower background radiation and higher cancer cell 18F-FDG uptake resulted in 3.7 times higher tumor SUV ( $1.8 \pm 0.6$ ,  $P = 0.008$ ) compared to reference condition while mice were not-anesthetized [23]. Figure 2-8 shows the tumor 18F-FDG uptake under different conditions.

In another study, Aliaga et. al. [24] used small animal PET imaging to screen the time-response of tumor metabolism to hormone and chemotherapy in a murine model of hormone-sensitive breast cancer. Small animal 18F-FDG PET imaging was used to evaluate tumor metabolic activity. Imaging was done before the administration of doxorubicin, methotrexate, letrozole, or placebo and also 1, 7, and 14 days after it. The 18F-FDG tumor uptake was calculated from a region-of-interest drawn around the tumor.

Aliaga et. al [24] investigated the effect of blood glucose level on the 18F-FDG uptake by tumor cells in mice ( $n = 48$  for MC4-L2 and  $n = 55$  for MC7-L1). Their tumor size ranged from 100 to 800 mm<sup>3</sup> and glucose levels were from 2.7 to 12.6 mmol/L. They observed a significant decrease (MC7-L1 slope =  $-0.63$ ; MC4-L2 slope  $-0.38$ ;  $p > 0.02$ ) in 18F-FDG tumor uptake with increasing glycemia, Figure 2-6. Considering these results, standardizing the blood glucose values before checking the results of treatment on 18F-FDG tumor uptake is necessary. To address this issue, they monitored the blood glucose level in a group of 10 tumor-free mice

fasted for a period of 24 hours. The blood glucose level fell rapidly after food removal and then leveled off as evidenced by the average glycemia values at 12 and 24 hours, which were not statistically different ( $p > 0.05$ ) [24]. As a result, they suggested a 12 hour fasting period for animals for the optimum effect of the blood glucose level on the  $^{18}\text{F}$ -FDG uptake by tumor cells in mice.

In another study, a group from PerkinElmer conducted a preclinical in vivo imaging on mice. Figure 2-9 shows  $^{18}\text{F}$ -FDG PET and CT images of two mice used to show the effect of fasting on  $^{18}\text{F}$ -FDG uptake in different organs. In the fasted mice (A),  $^{18}\text{F}$ -FDG uptake in the heart, brown fat and bowels was significantly ( $p < 0.01$ ) reduced in comparison with the non-fasted animals (B). As tumor cells preferably use glucose as an energy source, tumor  $^{18}\text{F}$ -FDG uptake remained similar or slightly improved after fasting (C). Nevertheless, fasting of animals improved overall image contrast by significantly reducing background  $^{18}\text{F}$ -FDG uptake in normal tissues such as brown fat ( $p < 0.0001$ ) and bowels ( $p < 0.001$ ) (C) [25].

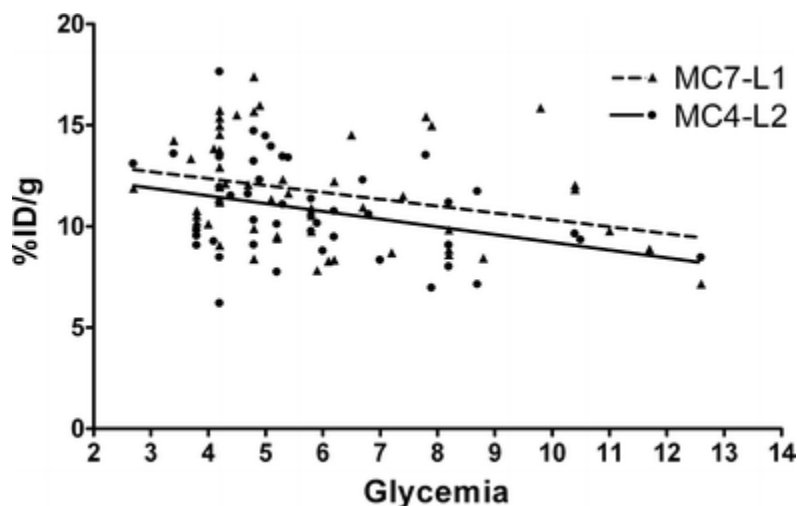


Figure 2-6- Tumor FDG uptake as a function of the blood glucose level for tumors MC7-L1 and MC4-L2 [24]. Reprinted by permission from Copyright Clearance Center: Springer Nature, Molecular Imaging and Biology, A Small Animal Positron Emission Tomography Study of the Effect of Chemotherapy and

Hormonal Therapy on the Uptake of 2-Deoxy-2-[F-18]fluoro-d-glucose in Murine Models of Breast Cancer, Antonio Aliaga, Jacques A. Rousseau, Jules Cadorette et al, 2007.

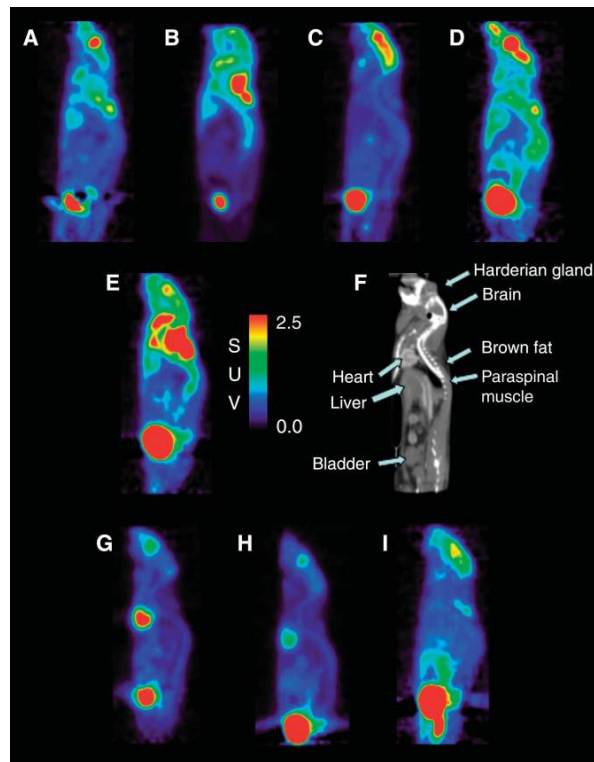


Figure 2-7- Examples of  $^{18}\text{F}$ -FDG biodistribution under different states. Images show sagittal sections through mice. For anatomic reference, a contrast-enhanced microCT scan is shown. (A) Not fasted, warmed, no anesthesia. (B) Fasted, not warmed, no anesthesia. (C) Fasted, warmed, no anesthesia. (D) Fasted, warmed, no anesthesia, conscious injection. (E) Reference conditions: not fasted, not warmed, no anesthesia. (F) microCT, sagittal view for anatomic reference. (G) Not fasted, warmed, isoflurane. (H) Fasted, warmed, isoflurane. (I) Fasted, warmed, ketamine. This research was originally published in JNM. B. J. Fueger, J. Czernin, I. Hildebradt, C. Tran, B. S. Halpern, D. Stout and et al, Impact of animal handling on the results of  $^{18}\text{F}$ -FDG PET studies in mice, J Nucl Med vol. 47, pp. 999 -1006, 2006. © SNMMI [23].

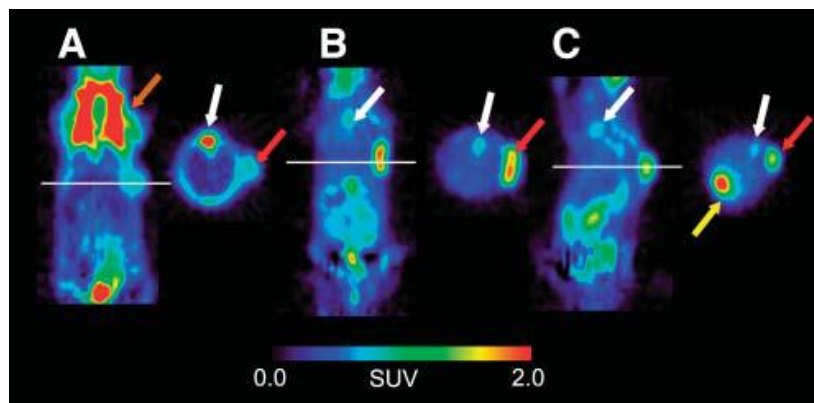


Figure 2-8- Tumor  $^{18}\text{F}$ -FDG uptake under various conditions. (A) Not fasted, not warmed, no anesthesia. (B) Fasted, warmed, no anesthesia. (C) Fasted, warmed, isoflurane anesthesia. Red arrow indicates tumor;

brown arrow indicates brown fat; white arrow indicates paraspinal muscle; yellow arrow indicates myocardium. This research was originally published in JNM. B. J. Fueger, J. Czernin, I. Hildebradt, C. Tran, B. S. Halpern, D. Stout and et al, Impact of animal handling on the results of  $^{18}\text{F}$ -FDG PET studies in mice, J Nucl Med vol. 47, pp. 999 -1006, 2006. © SNMMI [23].

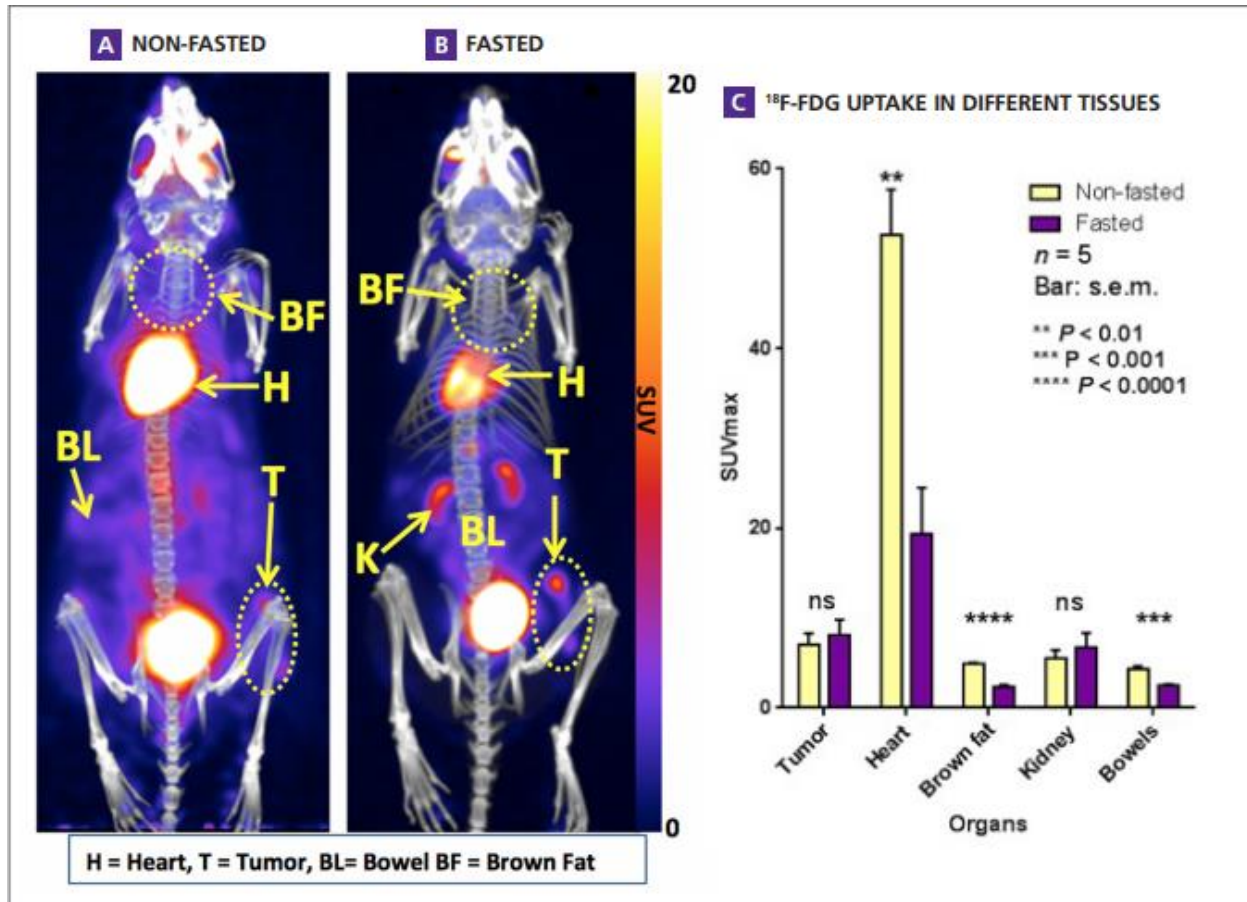


Figure 2-9- Food deprivation prior to PET imaging. This figure shows  $^{18}\text{F}$ -FDG PET and CT images of two representative mice used for this comparison. In the fasted mice (A),  $^{18}\text{F}$ -FDG uptake in the heart, brown fat and bowels was significantly ( $p < 0.01$ ) reduced in comparison with the non-fasted animals (B). As tumor cells preferably use glucose as an energy source, tumor  $^{18}\text{F}$ -FDG uptake remained similar or slightly improved after fasting (C). Nevertheless, fasting of animals improved overall image contrast by significantly reducing background  $^{18}\text{F}$ -FDG uptake in normal tissues such as brown fat ( $p < 0.0001$ ) and bowels ( $p < 0.001$ ) (C). Modest but not statistically significant increase in kidney uptake in fasting animals was observed, indicating active removal of excess tracer from the blood pool [25]. Reprint with permission from PrekinElmer Company.

## 2.5 Advantages of automated animal preparation tasks

As clarified earlier, animals' fasting before  $^{18}\text{F}$ -FDG PET imaging affects the background uptake level and consequently results in images with higher contrast level. To take advantage of

this fact, normally technicians in the animal facility at the University of Manitoba are responsible to remove the food from the animal's cage 6 to 8 hours before conducting PET imaging. This means that they must come to the animal facility in the middle of night to remove the food container from the animals' cage. In addition, it is essential to do follow up monitoring on the animals after the imaging to check on their health. As a result, all the mentioned animal handling leads to a high labor cost and time consumption. Furthermore, the presence of the technician disturbs the day and night 12 hour light/dark cycle of the animals.

To address the above issues and make the imaging research economically and scientifically more efficient, we designed and built a smart cage which automates the animal handling tasks and makes the remote monitoring possible.

To make clear the benefit of utilizing the smart cage, consider a research study that demands imaging of 8 mice in one day. If the desired fasting time for animal preparation is 6 hours, it means that the technician should remove the food access from the animals in the middle of the night. As Figure 2-10 shows, to set the fasting time exactly 6 hours the technician should repeat the food removal procedure hourly for eight mice. In addition to animal preparation, the technicians must check on the animals after imaging to make sure of they are still in good health and moving normally. This results in further time consumption by technician to check on the mice. As a result, the technician should work from 3 am to 8 pm, increasing the labor cost and potential for errors tremendously.









Animal #	Food removal time	Injection time	Image time	Follow-up check
 1	3:00	9:00	10:00	13:00
 2	4:00	10:00	11:00	14:00
 3	5:00	11:00	12:00	15:00
 4	6:00	12:00	13:00	16:00
 5	7:00	13:00	14:00	17:00
 6	8:00	14:00	15:00	18:00
 7	9:00	15:00	16:00	19:00
 8	10:00	16:00	17:00	20:00

Figure 2-10- An example case of imaging study including 8 mice. It shows the essential working hours for the technician to conduct the animal preparation, imaging and follow up checkups.

## 2.6 Motion detection algorithm

Nowadays motion detection algorithms are used widely for different applications including traffic control, security purposes and structural health monitoring. The most commonly used method to detect the object's motion is analyzing videos and images of the object recorded in a static location. For this purpose, different algorithms of image processing have been developed and applied over the years.

One of the main tasks of computer vision and image processing is foreground detection to detect changes in image sequences. To extract the foreground of an image a background subtraction technique is implemented. Background subtraction is used for traffic counting,

recording the number of people entering and leaving stores, and object and motion detection in general.

One of the most popular image processing packages is OpenCV, which is an abbreviation of Open Source Computer Vision. OpenCV is an open source computer vision and machine learning software library. OpenCV provides a common infrastructure for computer vision applications and to accelerate the use of machine perception in the products. It has different interfaces including C++, Python, Java and MATLAB and supports Windows, Linux, Android and Mac operating systems. [26]

There are different background subtractor functions in OpenCV based on different proposed algorithms which are reviewed in the following sections [26].

### **2.6.1 BackgroundSubtractorMOG**

The background subtractor function in OpenCV is a Gaussian Mixture-based Background/Foreground Segmentation Algorithm. P. KadewTraKuPong and R. Bowden [27] introduced this method in their paper "An improved adaptive background mixture model for real-time tracking with shadow detection" in 2001. It uses a method to model each background pixel by a mixture of K Gaussian distributions ( $K = 3$  to 5). The weights of the mixture represent the time proportions that those colours stay in the scene. The probable background colours are the ones which stay longer and more static [27].

### **2.6.2 BackgroundSubtractorMOG2**

BackgroundSubtractorMOG2 is also a Gaussian Mixture-based Background/Foreground Segmentation Algorithm. It is based on two papers by Z.Zivkovic, "Improved adaptive Gaussian mixture model for background subtraction" in 2004 [28] and "Efficient Adaptive Density

Estimation per Image Pixel for the Task of Background Subtraction" in 2006 [29]. The significant characteristic of this method is that it selects the proper number of Gaussian distributions for each pixel. It provides better adaptability to varying scenes due to illumination changes.

### **2.6.3 BackgroundSubtractorGMG**

BackgroundSubtractorGMG algorithm combines statistical background image estimation and per-pixel Bayesian segmentation. Andrew B. Godbehere, Akihiro Matsukawa, Ken Goldberg introduced this method in their paper "Visual Tracking of Human Visitors under Variable-Lighting Conditions for a Responsive Audio Art Installation" in 2012 [30].

This method uses the first few (120 by default) frames for background modelling. It employs probabilistic foreground segmentation algorithm that identifies possible foreground objects using Bayesian inference. The estimates are adaptive; newer observations are more heavily weighted than old observations to accommodate variable illumination. Several morphological filtering operations like closing and opening are done to remove unwanted noise. You will get a black window during first few frames [26].

## **2.7 Internet of things (IoT)**

Nowadays, one the most popular terms in technologies is internet of things. As Agenda describes, "The internet of things, or IoT, refers to a system of computing devices, analogue and digital machines, animals or people with unique identifiers that transfer data over a network without requiring constant human and computers interaction" [31].

A thing in internet of things can be anything ranging from small sensors to humans or animals. The data can be a recorded EKG signal, the body temperature of an animal in a farm in



Manitoba, deflection of a girder in a bridge, average number of cars passing through a cross section of highway in a month or the detected motion of an animal that is being monitored. All the objects or “things” in IoT are connected to a server or cloud through a network. Their static IP address which is assigned using their MAC address acts as a finger print for them.

In general, an IoT system includes a server or cloud system to store and analyze the collected data, required hardware to communicate with the target devices (gateways), and targets like sensors or actuators that are connected and controlled using a web-based program. The target devices send data along with their unique IDs to the cloud system through the gateways. The collected data can be analyzed on the cloud system itself or analyzed locally on a server machine. Also, they can receive controlling commands from the server through the gateways. These commands are the automatically generated commands using a developed program or direct ones which are sent by humans using the available user interface.

IoT applications are changing the world and animal handling is not an exception to this. There are different projects and research focusing on applying this technology to animal husbandry tasks. Xiong Benhai et. al. [32] reviewed the applications of Internet of Things technology in animal husbandry in China. They mentioned that this technology is used for controlling and adjusting animal farm equipment (draught fan, light, heater, water pump, etc.) based on analyzing the collected data from the installed sensors. In addition, a cloud system has been constructed to gather and analyze the data from thousands of cow-breeding and pig-breeding farms. The data are analyzed on this cloud system and provide useful tips to the farmer to improve the result. Furthermore, they mentioned that there is another application of IoT in this field which is the development and application of automatic electro-mechanical feeding control systems for lactating sows which was composed of electro-mechanical systems, wireless network

technology, mobile SQL Lite network database, electronic data interchange, and feed intake prediction models of lactating sow nutrient requirements [32].

In another report from the University of Cambridge and Centre for Digital Innovation, Zoetis, Mohammad Zaki et. al, [33] reviewed the opportunities and challenges of the internet of animal health things. They stated that the traditional animal production techniques are labor intensive and have slim margins. Considering the rapid human population growth, the traditional techniques do not meet the animal production goals for 2050. Therefore, through using the IoT in animals' health area and gathering and analyzing big data, we can improve these techniques and come up with better solutions [33].

# Chapter 3

## 3 Materials and methodology

To achieve our goal of automating the animal handling tasks for small animal PET imaging, we proposed to design and build a smart cage with following features:

- Automated food removal unit
- Remote monitoring module

In general, this project has three phases: 1) Design 2) Construction 3) Evaluation

In the design phase, we designed both hardware and software for the smart cage. The next step was constructing the designed hardware and implementing the software on it. At the end, we tested the smart cage in the animal facility at the University of Manitoba and evaluated its operation.

In the following sections of this chapter we will review the process of design and construction of each module.

### 3.1 The Smart cage requirements

In general, the first step in designing a system is to determine the requirements and limitations. The factors which were considered as requirements and limitation in the design of the smart cage are as below:

- 1) Affordability: We tried to keep the budget spent on each cage as low as possible and under 1000 CAD.

- 2) Portable: The cage must be designed in a way that could be easily carried and moved within the animal facility.
- 3) Water container: The cage must utilize the conventional water bottle used in cages throughout the animal facility.
- 4) Ease of use: Utilizing the cage software must be straightforward for the animal facility technicians and staff.
- 5) Low density cage: The cage's frame must be the same as the currently in use cages in the animal facility at the University of Manitoba, Figure 3-7.
- 6) Conform to University of Manitoba internet policy: The host PC that stores data and controls the smart cage, cannot be connected to a network other than university network via a router for information security purpose.
- 7) Disinfection compatibility: The added compartments must be cleaned and disinfected using autoclave or alcohol after each use.

All the involved tasks in design and construction of the smart cage are classified in two categories, hardware and software design. In the hardware section, the implemented components in the smart cage will be reviewed. Furthermore, the hardware interface and control system of each module will be explained in the software section.

## **3.2 Hardware**

Considering the smart cage's requirement and limitations, we started to design and build the hardware. Figure 3-1 shows a detailed diagram to clarify the communication between the components of the smart cage. In the following sections we will explain the properties and functionality of components utilized in the smart cage.

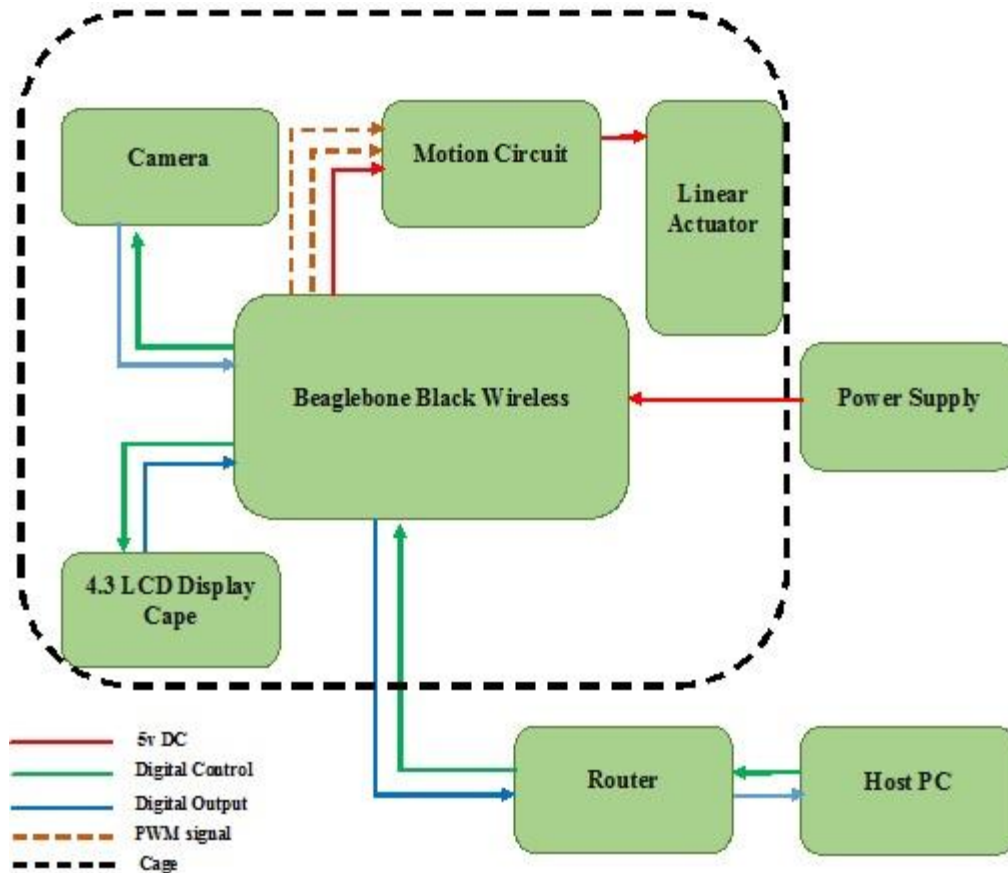


Figure 3-1- The functional diagram of the smart cage.

### 3.2.1 Beaglebone Black Wireless (BBBW)

To control different modules of the cage we used a Beaglebone Black Wireless, Figure 3-2. The Beaglebone Black Wireless is based on the open-source hardware design of the Beaglebone Black, created by the BeagleBoard.org Foundation. BBBW replaces the Ethernet interface of the Beaglebone Black with a high-performance WiFi/Bluetooth, WiLink interface manufactured by Texas Instruments. It has a serial debug port, a PC USB interface, and a USB 2.0 host port. Also, up to four expansion header boards or capes can be added to it. It has a high-performance TI ARM processor and supports a Debian or Ubuntu version of Linux [34]. Table 3-1 summarizes the specifications of the Beaglebone Black Wireless.

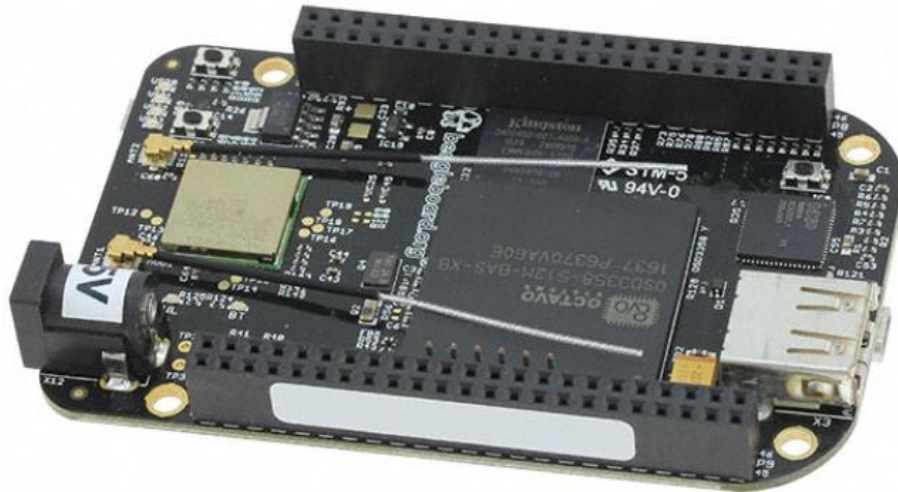


Figure 3-2- Beaglebone Black Wireless [35].

Table 3-1- Beaglebone Black Wireless specifications [32].

Feature	
<b>Processor</b>	Sitara AM3358BZCZ100 1GHz, 2000 MIPS
<b>Graphics Engine</b>	SGX530 3D, 20M Polygons/S
<b>SDRAM Memory</b>	512MB DDR3L 800MHZ
<b>Onboard Flash</b>	2GB, 8bit Embedded MMC
<b>Power Source</b>	miniUSB USB or DC Jack 5VDC External Via Expansion Header
<b>PCB</b>	3.4" x 2.1" 6 layers
<b>HS USB 2.0 Client port</b>	Access to USB0, Client mode via miniUSB
<b>HS USB 2.0 Host port</b>	Access to USB1, Type A Socket, 500mA LS/FS/HS
<b>Serial Port</b>	UART0 access via 6 pin 3.3V TTL Header. Header is populated
<b>SD/MMC connector</b>	microSD , 3.3V
<b>Connectivity</b>	WiLink 1835 802.11b/g/n 2.4GHz WiFi, Bluetooth, and Bluetooth Smart Module
<b>User Input</b>	Reset Button Boot Button Power Button

<b>Video Out</b>	16b HDMI, 1280x1024 (MAX) 1024x768,1280x720,1440x900 ,1920x1080@24Hz w/EDID Support
<b>Audio</b>	Via HDMI Interface, Stereo
<b>Software Compatibility</b>	Debian, Android, Ubuntu, Cloud9 IDE on Node.js w/ BoneScript library
<b>Weight</b>	39.68 grams

### 3.2.2 Linear actuator

To remove the food access from the animal, there must be a mechanism which open and close the located gate in front of the food container. For this purpose, an actuator that generates linear motion is essential. In addition, due to low weight of the gate, it can be a low power consumption actuator. Consequently, a linear actuator is the right device to meet all the requirements for closing and opening the gate of the food container.

A linear actuator is an actuator that creates motion in a straight line, in contrast to the circular motion of a conventional electric motor. An Actuonix L12-P linear actuator is utilized for moving the gate of the food container, Figure 3-3. The L12-P line of linear actuators feature an internal potentiometer for position feedback which is useful to control the motion of the food container gate. It has stroke length of 50mm that is adequate according to the food container design. It also has an input voltage of 6V [36].

To be able to reverse the motion of the linear actuator we created a simple circuit using a double-pole, double-throw (DPDT) switch. All the ports of the DPDT switch are connected to the BBBW to control the retraction and protraction of the actuator. As a safety precaution, the speed of protraction is much less than the retraction. If there is an obstacle while the food container's gate is closing, the actuator stalls. It will continue its motion after the obstacle is

removed. Figure 3-4 shows the schematic of the motion control circuit of the linear actuator. Table 3-2- Status of connected pins to the DPDT switch in linear actuator’s motion control circuit. The closing process of the gate is considered more slowly than its opening due to the animal’s safety.



Figure 3-3- L12-P micro linear actuator with position feedback [36].

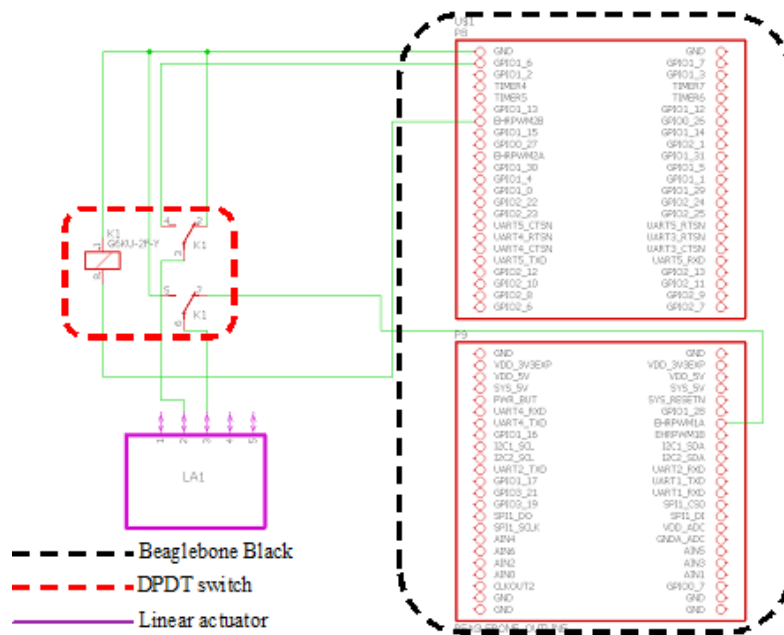


Figure 3-4- Linear actuator motion control circuit.

Table 3-2- Status of connected pins to the DPDT switch in linear actuator’s motion control circuit.

Pin number	Protraction (duty cycle=550)	Retraction (duty cycle=900)
P8.16	High	Low
P8.22	High	High
P9.42	High	High



### 3.2.3 Logitech C930e webcam

As mentioned earlier, one of the capabilities of the smart cage is remote monitoring of the animal during day and night. To monitor the cage during daylight we utilized a Logitech C930e HD web camera, Figure 3-5. The benefits of using this camera are as below:

- 1) It is a USB camera and can be connected to the USB port of the BBBW which is not occupied. Since the SPI ports of the BBBW are occupied with the LCD, we cannot use the other conventional SPI cameras. In addition, The USB interface speed is higher than SPI (480Mbps vs. 10Mbps).
- 2) It is a UVC (USB video class) camera meaning it is known as a USB camera in Linux operating system. As a result, it can be controlled with the Beaglebone Black Wireless which is the control unit on the cage.
- 3) It has a wide diagonal field of view, 90°, which allows the whole cage to be covered with it.
- 4) It is a low power consuming device and can be powered by the USB cable.



Figure 3-5- Logitech C930e webcam [37].

### **3.2.4 Reolink C1-pro IP Camera**

To be able to monitor the animal during night, a thermal camera or a night vision camera must be utilized. Due to the following reasons we chose an IP camera with night vision for remote monitoring during the night.

- 1) The lowest cost thermal camera we identified is the Flir Lepton camera, at 300 CAD. However, this device turned out to not be compatible with BBBW. It can communicate with a Windows operating host PC using a PureThermal board, costing 200 CAD, and still would require being wired to the host PC using a USB cable. As a conclusion, we decided to move away from a thermal camera and chose to work with a night vision camera instead.
- 2) IP cameras are easy to control and communicate with.

After considering the affordability and essential technical specifications of the camera for our project, we chose the Reolink C1-pro IP camera, Figure 3-6. It has a good night vision mode. In addition, it uses RTSP protocol and can be streamed using the VideoLAN Client (VLC) player.



Figure 3-6- Reolink C1-pro IP camera [38].

### 3.2.5 Cage's frame

The first step in the smart cage's design was to modify the cage frame currently in use to be able to locate all the essential devices and components in it. To keep the changes to the cage as minimal as possible to avoid distressing the animals, we only focused on redesigning the lid and the tray, which is seated on top of the cage's main body. All the devices and instruments are placed in the hollow space between lid and tray.

The 3D model of the cage was generated by acquiring an X-ray CT image of the cage and processing the CT data using InVesalius 3.0 software. The CT scan of the cage was performed in the PET/CT facility at the Health Sciences Center. Figure 3-8 shows the scan of the cage and the generated stl file of its 3D model. The exported 3D model then was used to draw the sketch of the lid and tray in a way to fit the main body of the cage.



Figure 3-7 The currently in use cage at the animal facility in the University of Manitoba.

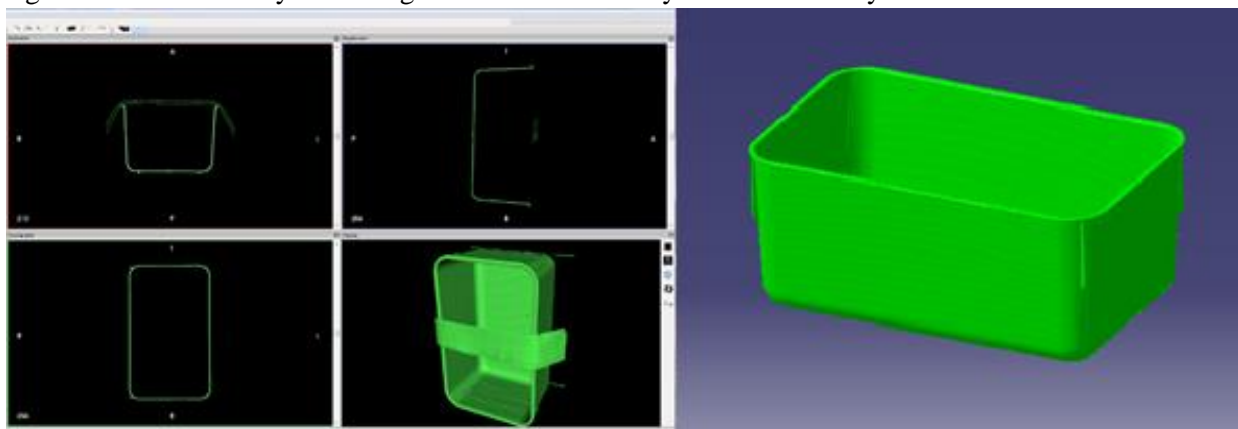


Figure 3-8- Generated 3D model of the main body of the existing cage in the animal facility at the University of Manitoba.

To build and manufacture the prototypes of the designed versions of the smart cage frame, a 3D printing method was chosen due to its simplicity and accessibility. The designed models are 3D printed using a Formlabs Form 2 3D printer at the PET imaging research lab. The Form 2 is a Stereolithography (SLA) 3D printer by Formlabs Company. Table 3-3 is a summary of specifications of the Form 2, the printing setting for printing the models and the material used. Due to small size of the build platform of Form 2 3D printer, it was not possible to build the large compartments of the smart cage. Therefore, the largest parts were first manufactured in the 3D printing facility of the Medical Physics department at University of Manitoba. These parts

were made of ABS material, Figure 3-15. After testing the initial designs and applying the essential revisions to the model, the largest compartments of the smart cage were 3D printed in the OIC Precision Laboratories using a Fortus 400mc 3D printer. These parts were made of ABS material, Figure 3-14 and Figure 3-18.

Table 3-3- A summary of specifications of the Form 2, the printing setting for printing the models and the used material [31]

<b>Formlabs Form 2</b>	
<b>Technology</b>	Stereolithography (SLA)
<b>Peel Mechanism</b>	Sliding peel process with wiper
<b>Build Volume</b>	145 × 145 × 175 mm
<b>Layer Thickness</b>	25, 50, 100 microns (100 microns layer thickness was used to print the models)
<b>Laser Spot Size (FWHM)</b>	140 microns
<b>Material</b>	Clear Formlab resin
<b>Fortus 400mc</b>	
<b>Technology</b>	FDM
<b>Build Volume</b>	40.6 x 35.5 x 40.6 cm
<b>Layer Thickness</b>	330 microns
<b>Material</b>	ABS plastic

The following compartments were designed, and 3D printed to fit different modules of the smart cage.

### **1. Food container**

In the conventional cages which are in use of the animal facility, the food pellets are located on a steel mesh frame which is placed on the main body of the cage. However, in the smart cage design, the food pellets are stored in a container with a movable gate. A mesh frame was placed in the front panel of the food container to keep the food in the enclosed area. In addition, the base of the container is inclined to make sure of the food accessibility to the animal. Figure 3-9 shows

the 3D model of designed food container and Figure 3-10 shows the 3D printed prototype of that model.

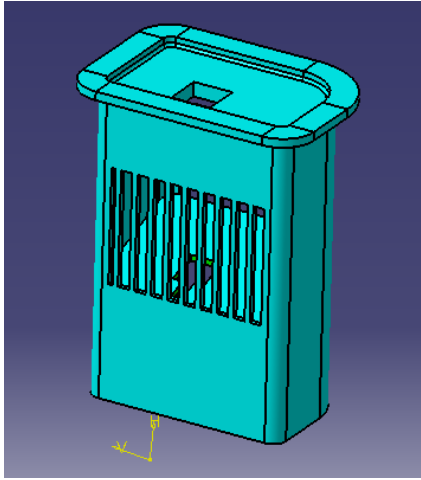


Figure 3-9- The 3D model of designed food container for the smart cage. It has a tilted base to make sure of food accessibility to the mouse. The food window is placed above the ground to avoid trapping the mouse tail. The rectangular hole on top of the container is for mounting the linear actuator that controls the food access window.

Figure 3-10- 3D printed food container.

## 2. Tray

As mentioned earlier a tray was designed to be seated on top of the cage's main body for locating the components. Its net plate design allows the required air flow in the cage and prevents the animal's contact with electronics component. Figure 3-12 shows First version of designed and 3D printed model of the tray. This prototype is printed using a Formlabs Form 2 3D printer. Due to small size of build platform of Formlabs Form 2 3D printer, the model has been cut to four pieces. Each piece was printed individually. Finally, four 3D printed pieces were attached together using spare clear resin and UV light which produces strong bonding. This

model has 8mm×8mm mesh size that is too large for preventing the mouse from accessing the components on the tray. In addition, the water bottle space is not large enough to store the required water for the mouse. The thickness of the tray in this model is 1 cm which has been reduced in the next versions. After consulting with Dr. Mike Jackson, the coordinator of the animal facility at University of Manitoba, this model has been revised and changed as shown in Figure 3-11. Figure 3-11 shows the 3D model of the designed tray for mounting the essential components of the smart cage. A) The specified location for mounting the food container. B) The location of mounting the water bottle. C) The location of mounting the day camera. Figure 3-13 shows the 3D printed prototype of this model. This prototype is also printed by a Formlabs Form 2 3D printer using clear resin. It did not fit in the Formlabs Form2 3D printer as well as the first version. All the previous steps in the manufacturing of the first version were repeated. In this model the mesh size reduced to 4mm×4mm. The located spot for water bottle has been changed according to the existing water bottle in the animal facility at University of Manitoba. In this design the water bottle is located on top of the tray instead of inside the cage. The camera spot is covered with a plexi glass to prevent mouse from getting outside the cage. To consume less amount of resin, the thickness of the tray is reduced to 3 mm. The strength of the tray was tested in a period of 6 months while all the components were located on it. After testing this version in the animal facility at University of Manitoba, the third version of the tray was designed which was almost the same as the second one. This model as shown in Figure 3-14, is printed with a different 3D printer, Fortus 400mc, at the OIC Precision Laboratories in one piece using ABS plastics. When the tray was 3D printed in pieces and made from resin, each piece showed a warpage around the edges. This comes from the small thickness of the tray compared to the other dimensions. In addition, since the model was printed in four pieces, dealing with this warpage

was more difficult. To solve this issue, as explained earlier, the 3<sup>rd</sup> version was made from ABS plastics and using a different device.

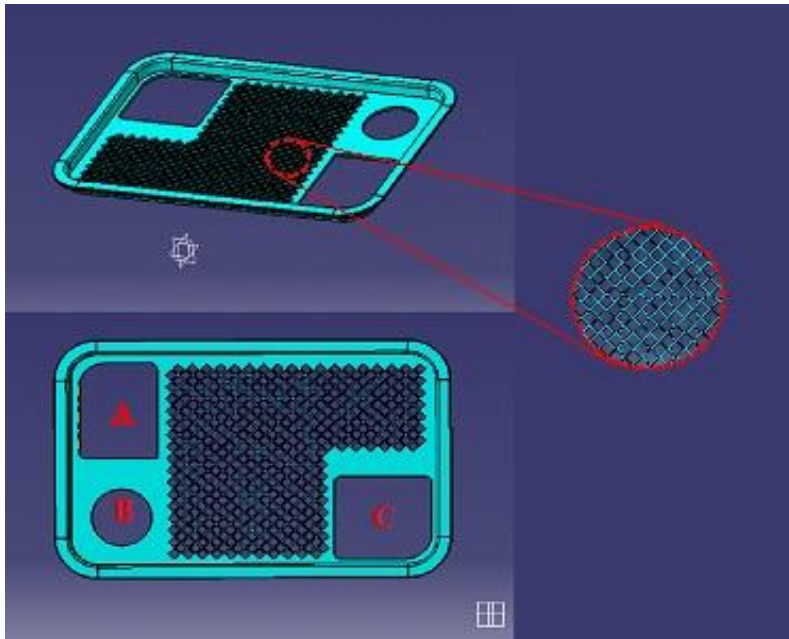


Figure 3-11- The 3D model of the designed tray for mounting the essential components of the smart cage. A) The specified location for mounting the food container. B) The location of mounting the water bottle. C) The location of mounting the day camera.

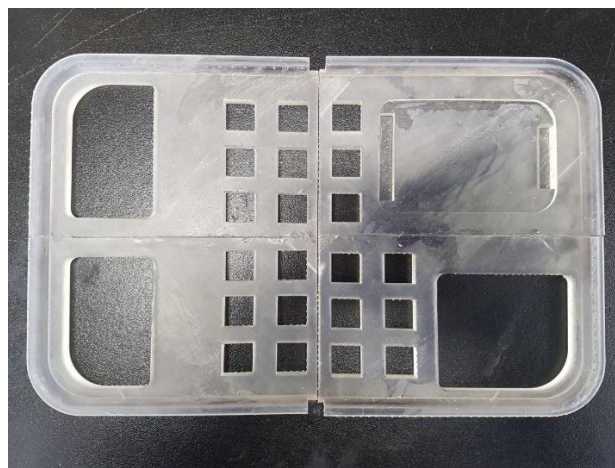


Figure 3-12- The first version of designed and 3D printed model of the tray. This prototype is printed by a Formlabs Form 2 3D printer using clear resin. This model has 8mm×8mm mesh size that is too large for preventing the mouse from accessing the components on the tray. In addition, the water bottle space was not large enough to store the required water for the mouse. The thickness of the tray in this model was 1 cm which has been reduced in the next versions.



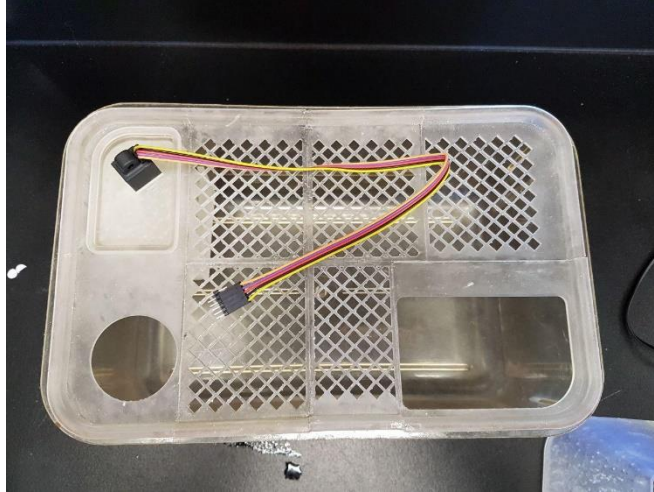


Figure 3-13- Second version of designed and 3D printed model of the tray. This prototype is printed by a Formlabs Form 2 3D printer using clear resin. In this model the mesh size reduced to 4mm×4mm. The located spot for water bottle has been changed according to the existing bottle water in the animal facility at University of Manitoba. In this design the water bottle is located on top of the tray instead of inside the cage. The camera spot is covered with a plexi glass to prevent mouse from getting outside the cage.



Figure 3-14- The 3D printed prototype of the designed tray for the smart cage. This prototype is printed with a different 3D printer, Fortus 400mc, at the OIC Precision Laboratories in one piece using ABS plastics.

### 3. Lid

The lid of the cage was modified in a way to hold a capacitive touch screen LCD on it as a user interface. Figure 3-15 shows the first model of the designed lid. These parts were printed in the 3D printing facility of Medical Physics department at University of Manitoba due to their

large size. In the first design, the water bottle was considered to be located inside the main cage's frame. However, after consulting with Dr. Michael Jackson, this model was revised to the second version which is shown in Figure 3-16. In this version, the water bottle was considered to be located on top of the tray. After testing the smart cage with the designed lid, the third version of the lid was designed and manufactured, Figure 3-17 and Figure 3-18. The new consideration in this design was separating the water bottle from the other components on the tray to avoid having water droplets fall on moisture sensitive components while the user puts the bottle on the tray. The third model was 3D printed with a Fortus 400mc 3D printer using ABS plastics. A warpage in the lid walls were observed when it was printed with Form 2 3D printer with the same reasons that were explained in the previous section. To avoid this warpage and being able to print the whole model in one piece, this part was built using another 3D printer as mentioned earlier.

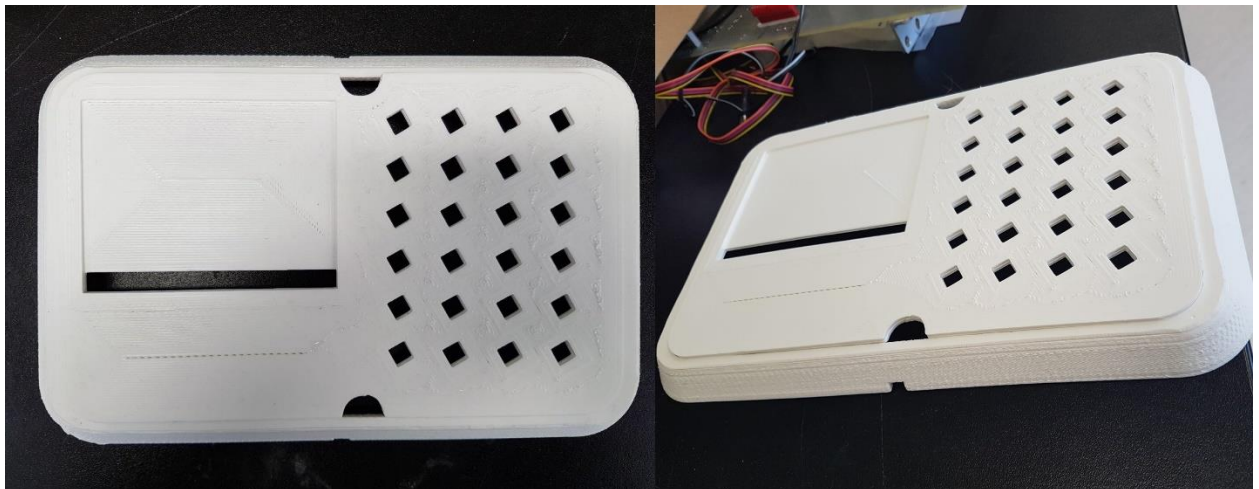


Figure 3-15- The first version of designed and 3D printed model of the lid. This is the first model of the designed lid. These parts were printed in the 3D printing facility of Medical Physics department at University of Manitoba due to their large size. They are made of ABS plastics. In the first design, the water bottle was considered to be located inside the main cage's frame. A capacitive touch screen LCD was considered to be located on the lid as user interface.

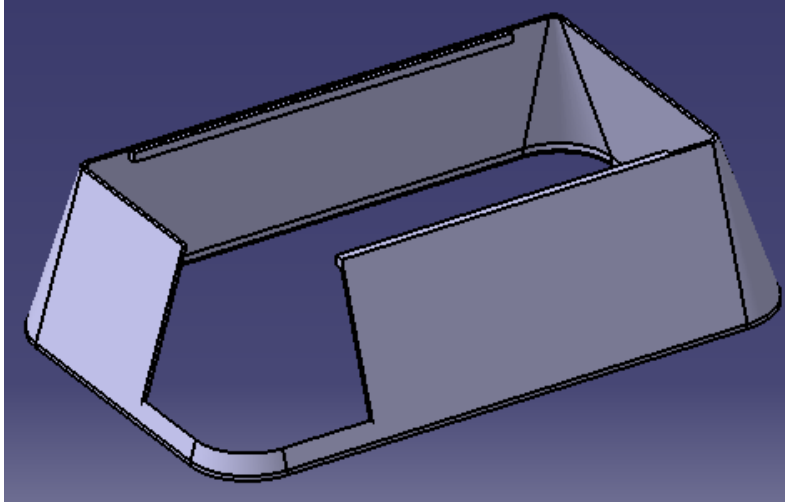


Figure 3-16- The second version of the designed and 3D printed model of the lid. In this design, the water bottle was considered to be placed on top of the tray. Consequently, the height of the lid was increased to cover the lateral load of the water bottle to prevent it from falling on other components of the smart cage.

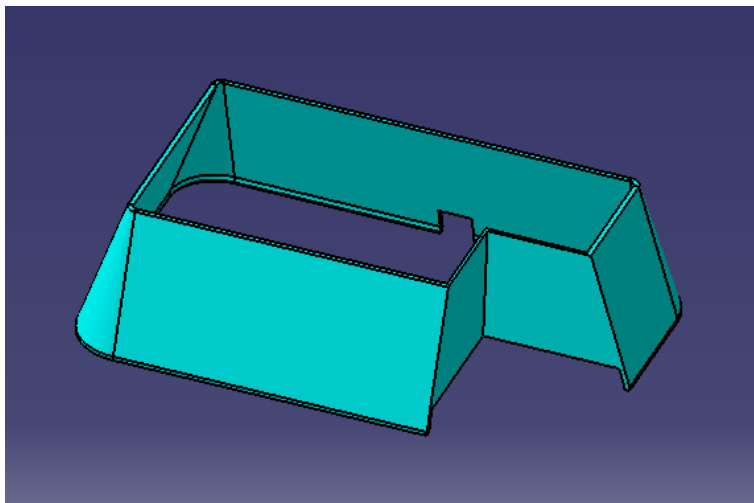


Figure 3-17- The 3D model of the designed lid for the Smart cage. The new consideration in this design was separating the water bottle from the other components on the tray to avoid having water droplets fall on moisture sensitive components while the user puts the bottle on the tray.

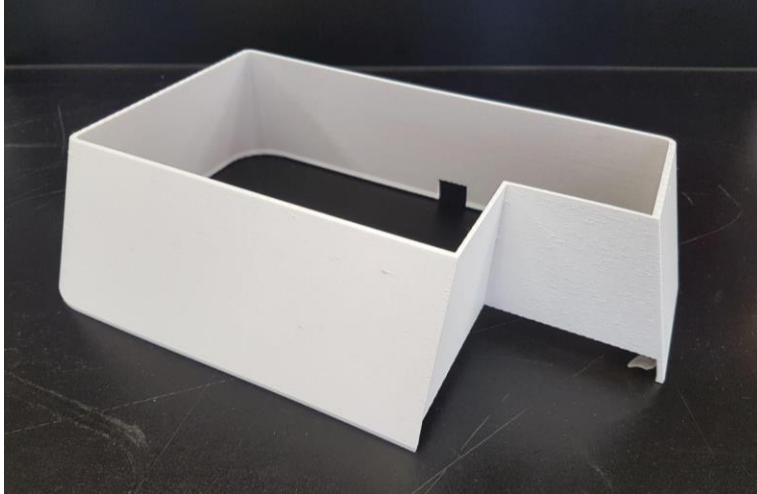


Figure 3-18- The 3D printed prototype of the designed lid for the smart cage. This model was 3D printed with a Fortus 400mc 3D printer at the OIC Precision Laboratories using ABS plastics. A warpage in the lid walls were observed when it was printed with Form 2 3D printer. To avoid this warpage and being able to print the whole model in one piece, this part was built using another 3D printer.

### 3.4 Software

To be able to control the available modules in the smart cage, a software interface is essential. As mentioned earlier, all of the smart cage's modules are controlled using a control unit on the cage that is a microcomputer, the Beaglebone Black Wireless. This microcomputer communicates with a host computer on a local network to send the data and receive commands from users. The user can remotely customize the cage's setting using a GUI software on the host computer. In addition, the user can program the cage directly using a touch screen LCD located on its lid. Figure 3-19 shows the smart cage software diagram that explains the communications between different sections of the software. Figure 3-20 illustrates the network diagram of the smart cage. As Figure 3-20 shows the host PC and the smart cages communicate with each other using a router. For this project, a D-link router has been used. Maximum of twenty cages can communicate with the host PC using this router.

In the following sections the design and implementation of developed software packages to control the smart cage's modules are explained.

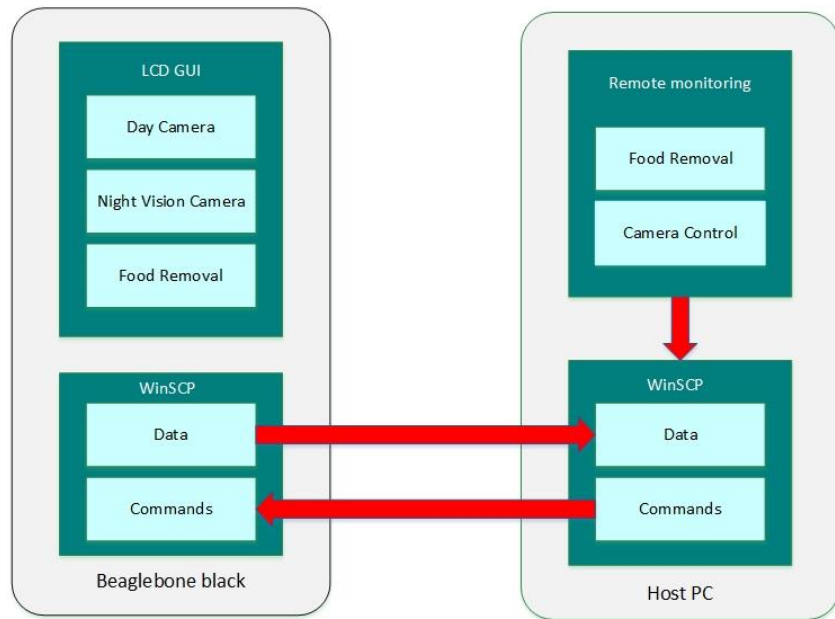
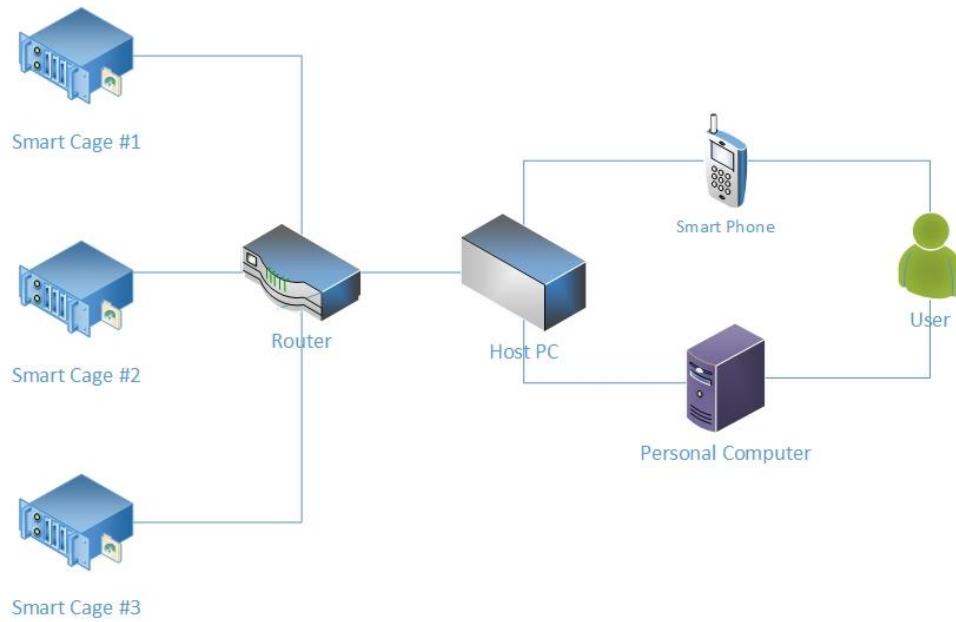


Figure 3-19- Software diagram of the smart cage.



Detailed network diagram

Figure 3-20- Network diagram of the smart cage

### 3.4.1 Beaglebone Black Wireless software

The Beaglebone Black Wireless includes either a 2GB or 4GB on-board eMMC flash memory chip. It comes with the Debian Linux distribution factory pre-installed [34]. We flashed the eMMC memory chip and installed the 8.7 version of Debian Jessie on it. The reason for choosing this version is its corresponding kernel version is the 4x version. In the 4x version of the kernel, a more reliable version of Capemgr package is installed. Capemgr was created out of a need for boards like the Beaglebone Black to be able to detect installed expansion boards at boot time and allocate appropriate resources (load drivers, allocate GPIO, reserve bus addresses, etc.) on kernels which use Device Tree. Capemgr is completely implemented in the kernel. Each cape is represented by a single DTS (Device Tree Source) fragment file. At kernel build time, these fragments are compiled by the Device Tree Compiler into dtbo files (Device Tree Blob Object). At install time, these dtbo objects are copied to `/lib/firmware` [39]. The loaded capes on the

BBBW in this project include a 4.3"-LCD-cape and a cape\_universala. Cape-universala exports all pins used by HDMI and eMMC so we can configure the remaining available pins which are not used by LCD.

As mentioned earlier, Beaglebone Black Wireless has a 512 MB DDR3 RAM which is not sufficient for installing different large size libraries on it. Therefore, its file system partition has been expanded on a 16 GB micro SD card.

To be able to use the LCD as a user interface, the first step is to have an operating system that supports a desktop environment. For this purpose, we installed an LXQT, a lightweight Qt desktop environment on the BBBW. It is focused on being a classic desktop with a modern look and feel. Historically, LXQt is the product of the merge between LXDE-Qt, an initial Qt flavour of LXDE, and Razor-qt, a project aiming to develop a Qt based desktop environment with similar objectives as the current LXQt [40].

To use the touchscreen LCD as a keyboard, Florence package was installed along with "at-spi2-core" package for Debian on the BBBW, Figure 3-21. Florence is an extensible scalable virtual keyboard for X11. The At-Spi2 Core package is a part of the GNOME Accessibility Project. It provides a Service Provider Interface for the Assistive Technologies available on the GNOME platform and a library against which applications can be linked [41].



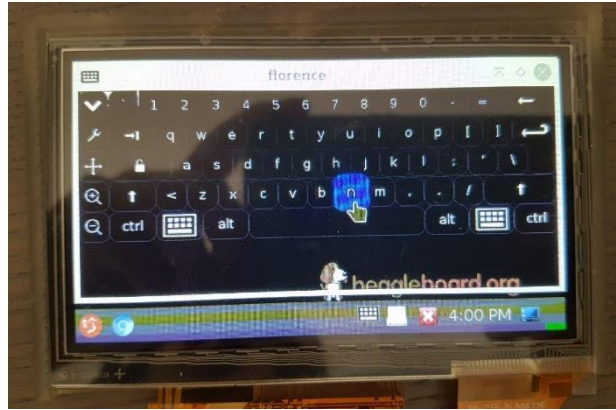


Figure 3-21- The virtual Florence keyboard package installed on BBBW.

To adjust the settings of different modules of the smart cage directly, we have created a graphical user interface (GUI) using Tkinter package in Python. Two different GUIs have been created to control food removal and camera module. Using the FoodRemoval program, users can set the schedule for food removal. Further, users can record videos and capture images using the Camera program on the BBBW. Figures 3-22 to 3-29 show the designed icons of the GUIs and their environments.



Figure 3-22- Designed icon for FoodRemoval program GUI.



Figure 3-23- Designed icon for Camera module's program.



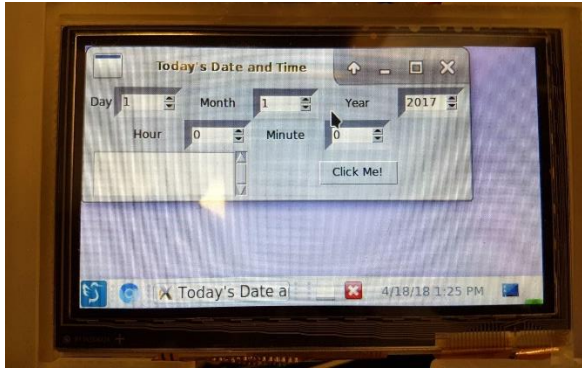


Figure 3-24- FoodRemoval module's GUI, setting today's date and time.



Figure 3-25- Camera module's GUI.

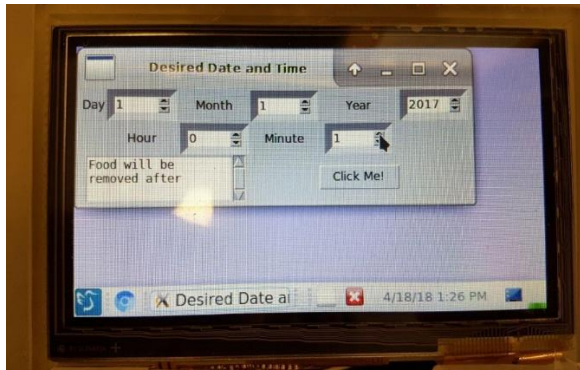


Figure 3-26- FoodRemoval module's GUI, setting desired date and time to remove food.

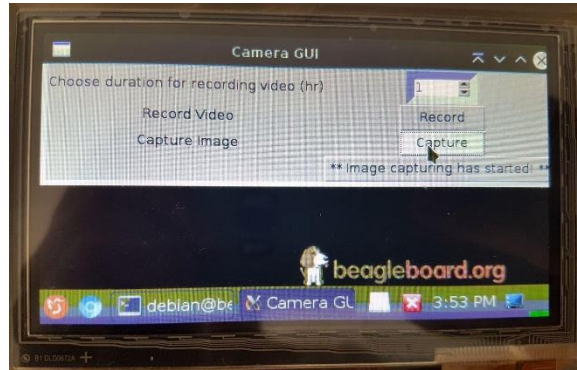


Figure 3-27- Camera module's GUI. Capturing images with 1 frame per minute rate for 1-hour duration.

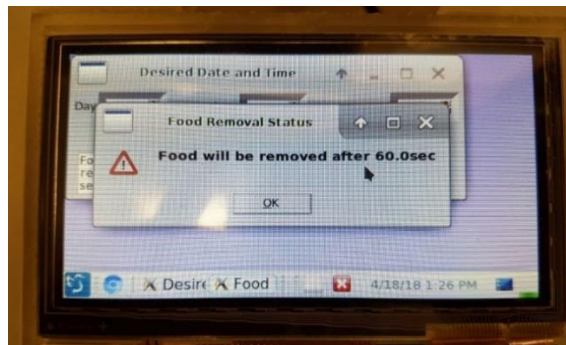


Figure 3-28- FoodRemoval module's GUI, Showing the remaining time to remove food from the cage.

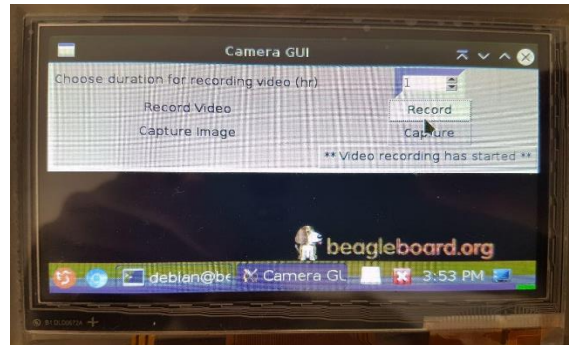


Figure 3-29- Camera module's GUI. Recording video with 10 frames per second rate for 1-hour duration.

### **3.3.2 Host PC software**

To be able to control the cage remotely through a host PC, software was created using National Instruments LabWindows/CVI. In the following sections we will introduce the software developed for the Host PC.

#### **LabWindows CVI**

National Instruments LabWindows/CVI is an ANSI C integrated development environment and engineering toolbox with built-in libraries for measurement, analysis, and engineering UI design [42].

The created software has three general sections as shown in Figure 3-30.

- 1) In the first section, the user chooses which smart cage is going to be set. Considering the properties of the router, twenty smart cages can connect to the created Local Network. Each cage is identified by the assigned static IP address according to the MAC address of its BBBW.
- 2) The second section of the software is assigned to the food removal module. In this section the user enters the desired time to remove food access from the animal. The remaining time until food is to be removed is shown in the same window. There is a default setting for this section that make sure of the animal's food access after 6 hours of fasting. This special situation was considered to avoid starving the animal in case the imaging has been canceled and the technician has forgotten to open the gate of the food container.
- 3) The last section is assigned to the camera module. The user can record videos, capture images, view the recorded videos and captured images, watch a live stream from the cage and observe the motion history of the animal in a graph.

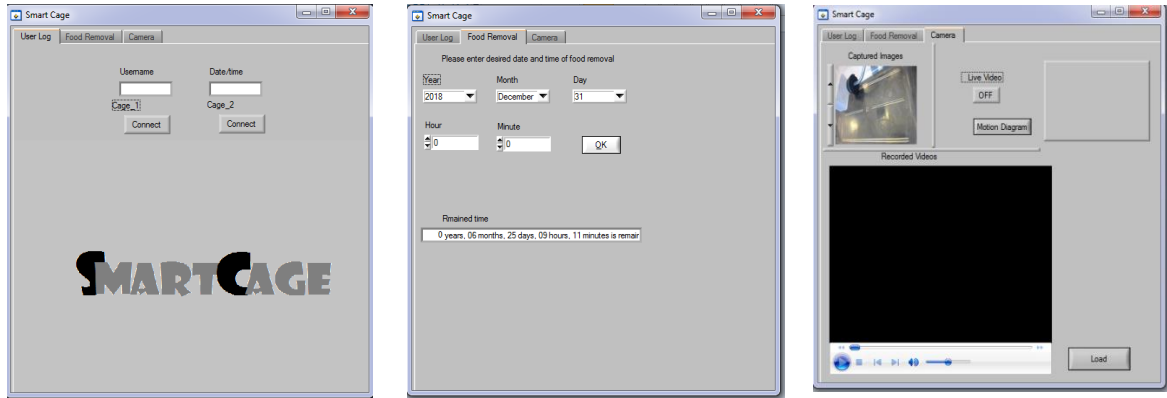


Figure 3-30- Host PC user interface.

## WinSCP

The communication between BBBW and host PC is established using WinSCP software. WinSCP is an open source free SFTP client, FTP client, WebDAV client, S3 client and SCP client for Windows. Its main function is file transfer between a local and a remote computer. Beyond this, WinSCP offers scripting and basic file manager functionality. Using the scripting, all the recorded data are transferred to the host PC. In addition, we remotely command the BBBW using this by sending the executable bash scripts to it. This communication is established using the SCP protocol. To run the WinSCP specific files and commands we wrote batch files which are integrated with the user interface program. [43]

## Motion detection and tracking algorithm

To reduce the time spent by the technician to review all the recorded videos and captured pictures to observe the animal's movements, we designed and implemented a motion detection and tracking algorithm into the microcomputer of the smart cage. The program is written in the python language using the functions of the OpenCV library.

As explained in Chapter 2 the most common and simplest method among motion detection techniques is background subtraction or said in another way, foreground detection. The

algorithm implemented for motion detection in the smart cage uses the same method. The major reasons to choose this method are its simplicity, low processing time, and good response when the background is static. In the case of the smart cage, the background of the room at the animal facility is quite static. Since the light level does not change until 6 pm in the evening, the variance of the light intensity would not affect the result.

After grabbing the first frame, its size is compressed to 500x500 pixels. The reason for this compression is the high processing time required for image processing with the original size of frames, 1920x1080. It's important to understand that even consecutive frames of a video stream will not be identical. Due to tiny variations in the digital camera sensors, no two frames will be 100% the same, some pixels will most certainly have different intensity values [44]. Therefore, a Gaussian smoothing was applied to average pixel intensities across a  $21 \times 21$  region. This helps smooth out high frequency noise that could throw our motion detection algorithm off. For modelling the background frame, an adaptive background subtractor function was applied. The background frame is an average of the last 50 frames of the recorded video. While the first 50 frames are recording, the first grabbed frame is assumed as the background and is subtracted from the other frames. After calculating the area that has changed during the current frame, its boundary is generated. To be able to produce a set of understandable and easy to follow graphs of the mouse motions the coordinates of the center of the generated area are recorded and plotted during the time. As a result, two graphs corresponding to motions in x and y directions are produced.

# Chapter 4

## 4. Results

As mentioned in the previous chapter, there were some considerations and limitations which determined our design policy. To evaluate the performance of the constructed smart cage, we should check if all the essential needs are met. In the following section we will evaluate the cage's performance thoroughly. In general, we will review the smart cage's performance in two categories of hardware and software. In addition, the smart cage has been tested in the animal facility at the University of Manitoba. All testing that involved animal subjects was conducted under an animal use protocol approved by the Animal Care Committee of the University of Manitoba and in compliance with Canadian Council on Animal Care (CCAC) and University of Manitoba policies.

### 4.1 Hardware evaluation

According to Mitchell, the performance of a newly designed hardware can be evaluated considering the following criteria, Table 4-1 [45]:

Table 4-1- Criteria defined for evaluating the hardware of the smart cage [45].

<b>Criteria definition</b>	
<b>Mass</b>	The physical weight of the hardware interface
<b>Cost</b>	The cost of test, evaluation, manufacture, and assembly
<b>Maintainability</b>	The potential maintenance time, including servicing repair
<b>Housekeeping</b>	The time required to clean each type of interface
<b>Durability</b>	The ability of the hardware to withstand
<b>Potential</b>	The variety of ways in which the hardware accommodates
<b>Operation</b>	the ease and speed of attaching and detaching hardware

### 4.1.1 Mass

As described in the design section, the equipment and components of the smart cage will be seated on a tray above the cage's main body. Therefore, the mass of the components should be tolerable by the designed tray and the base frame. In Table 4-2, you can find the weight of all the components of the smart cage. As Table 4-2 shows the water bottle is the heaviest component and will be seated at one corner of the tray. As a result, it is well supported by the base frame and the produced moments by its weight becomes minimum.

Table 4-2- The components' weight of the smart cage.

Components name		Weight (g)
Food container (empty)		100
Removable gate of the food container		10.5
Tray		100
lid		200
LCD		100
BBBW		42
Motion control circuit		30
Water bottle	Empty	451
	Full	1151
Total weight		1733.5

### 4.1.2 Cost

One of the major points in designing new device is its affordability. Table 4-3 **Error! Reference source not found.** shows the cost of test, evaluation, manufacture, and assembly of the components of the smart cage.

Table 4-3- The cost of test, evaluation, manufacture, and assembly of the smart cage's components.

Components name	Price (CAD)
-----------------	-------------

<b>BBW</b>		88 \$
<b>4.3" LCD Capacitive Touchscreen Display Cape</b>		60 \$
<b>Logitech C930e webcam</b>		170 \$
<b>Reolink C1-pro IP camera</b>		110 \$
<b>DPDT switch</b>		5 \$
<b>3D-printed frame and components</b>	Resin	83 \$
	ABS	170 \$
<b>Total cost</b>		773

### 4.1.3 Housekeeping

One of the major demands of the animal facility at the University of Manitoba is to be able to sterilize and clean cage components. We 3D-printed all the additional compartments of the cage's frame using Acrylonitrile-Butadiene-Styrene (ABS) material and resin. Table 4-4 to 4-7 show the solvent compatibility and mechanical properties of the clear resin and ABS material.

Table 4-4- Mechanical properties of the Formlab clear resin [31].

<b>Mechanical properties<sup>1</sup></b>	<b>Green<sup>2</sup></b>	<b>Postcured<sup>3</sup></b>	<b>Method</b>
<b>Tensile Properties</b>			
Ultimate Tensile Strength	38 MPa	65 MPa	ASTM D 638-10
Young's Modulus	1.6 GPa	2.8 GPa	ASTM D 638-10
Elongation at Failure	12%	6.2%	ASTM D 638-10
<b>Flexural Properties</b>			
Flexural Modulus	1.25 GPa	2.2 GPa	ASTM C 790-10
<b>Impact Properties</b>			
Notched IZOD	16 J/m	25 J/m	ASTM D 256-10
<b>Temperature Properties</b>			
Heat deflection temp. @ 264 psi	42.7 °C	58.4 °C	ASTM D 648-07
Heat deflection temp. @ 66 psi	49.7 °C	73.1 °C	ASTM D 648-07

Table 4-5- Solvent compatibility of Formlab clear resin. Percent weight gain over 24 hours for a printed and post-cured 1 x 1 x 1 cm cube immersed in respective solvent [31].

<b>Mechanical Properties</b>	<b>24 HR WEIGHT GAIN (%)</b>
Acetic Acid, 5 %	< 1
Acetone	sample cracked

<sup>1</sup> Material properties can vary with part geometry, print orientation, print settings and temperature.

<sup>2</sup> Data was obtained from green parts, printed using Form 2, 100 µm, Clear settings, without additional treatments.

<sup>3</sup> Data was obtained from parts printed using Form 2, 100 µm, Clear settings and post-cured with 1.25 mW/cm<sup>2</sup> of 405 nm LED light at 60 °C for 60 minutes.

Isopropyl Alcohol	< 1
Bleach, ~5 % NaOCl	< 1
Diethyl glycol monomethyl ether	1.7
Hydraulic Oil	< 1
Skydrol 5	1
Hydrogen Peroxide (3 %)	< 1
Isooctane	< 1
Salt Water (3.5 % NaCl)	< 1
Sodium hydroxide (0.025 %, pH = 10)	< 1
Water	< 1
Xylene	< 1
Strong Acid (HCl Conc)	distorted

Table 4-6- Mechanical properties of ABS material [46].

<b>Mechanical properties</b>		<b>Method</b>
<b>Tensile Properties</b>		
Ultimate Tensile Strength	42.5 - 44.8 MPa	ASTM D 638
Young's Modulus	2 - 2.6 GPa	ASTM D 638
Elongation at Failure	23 - 25 %	ASTM D 638
<b>Flexural Properties</b>		
Flexural Modulus	2.25 – 2.28 GPa	ASTM C 790
<b>Impact Properties</b>		
Notched IZOD	24.6 - 29.4 J/m	ASTM D 256
<b>Temperature Properties</b>		
Heat deflection temp. @ 264 psi	88 °C	ASTM D 648
Heat deflection temp. @ 66 psi	93.8 °C	ASTM D 648

Table 4-7- Solvent compatibility of ABS material [39].

<b>Mechanical Properties</b>	<b>24 HR WEIGHT GAIN (%)</b>
Acetic Acid, 10 %	No data available
Acetone	Not resistant
Isopropyl Alcohol	Resistant
Bleach, ~5 % NaOCl	Not resistant
Butyl Acetate	Not resistant
Diesel	No data available
Diethyl glycol monomethyl ether	Not resistant
Hydrogen Peroxide (3 %)	Resistant under 80°C
Isooctane	No data available
Mineral Oil	Not resistant above 100°C
Sea Water	Resistant under 60°C
Sodium hydroxide (20%)	Resistant under 60°C
Water	Resistant



Xylene	Not resistant
Hydrochloric acid 37%	Resistant under 20° C

#### **4.1.4 Durability**

Durability is the ability of a physical product to remain functional, without requiring excessive maintenance or repair, when faced with the challenges of normal operation over its design lifetime.

Durability can incorporate several specific physical properties of designed products, including: 1) Resistance to fatigue, 2) Radiation hardening, 3) Thermal resistance, 4) Toughness, 5) Waterproofing.

According to Table 4-6 and Table 4-7, the 3D-printed compartments are durable in the condition in which it will be utilized since there is no high tension or compression. In addition, the loading on the cage will not be a cyclic high frequency one.

#### **4.1.5 Potential**

The variety of ways in which the hardware accommodates different configurations and adapts to use in many areas is the definition of the potential in the device performance concept. The smart cage is designed and constructed in a way that the other options and modules can be added to it to meet more functional goals. One of the considered options to be developed is controlling several smart cages through the host PC user interface. There is a specified section in the code which can be further developed for adding more than one cage in the future.

## 4.2 Software evaluation

The evaluation of the developed software has been done according to Table 4-8. One of the major considerations while designing the user interface for the smart cage was its ease of use. To meet this goal, a user manual for the smart cage has been created. In addition, the installation requirements and process of the smart cage’s software are explained in its readme file.

To be able to develop the smart cage further, the written programs are commented and fully explained. Furthermore, all the issues and errors we encountered during the project are recorded along with their solutions to make the future work simpler.

Table 4-8- The software evaluation criteria [40].

<b>Criterion</b>	<b>Sub-criterion</b>	<b>Notes – to what extent is/does the software...</b>
<b>Usability</b>	Understandability	Easily understood?
	Documentation	Comprehensive, appropriate, well-structured user documentation?
	Installability	Straightforward to install on a supported system?
	Learnability	Easy to learn how to use its functions?
<b>Sustainability and maintainability</b>	Identity	Project/software identity is clear and unique?
	Changeability	Easy to modify and contribute changes to developers?
	Evolvability	Evidence of current/future development?

## 4.3 Automating food removal

One of the major demands of the animal facility at the University of Manitoba was automating the food removal procedure to reduce labor cost and time consumption. As explained in Chapter 3, an electrical linear actuator, controlled by the host PC is utilized to automate this process. One of the arising questions was whether opening and closing the gate of the food container leads to distressing the mouse.

According to the Committee on Recognition and Alleviation of Distress in Laboratory Animals, National Research Council of the United States of America, the short term symptoms

of distressing the mouse include acute urinating and staying at the corner of the cage [47]. None of the mentioned short term symptoms were noticed during testing the unit in the animal facility at the University of Manitoba. The mouse moved around the cage. It stayed close to the food container unit when the gate was closing and opening. In addition, no sign of acute urination has been observed during the test.

Figure 4-1 shows the area the covered area by the Logitech web camera seated on the tray. By locating it at a special angle the whole cage's floor area can be seen. Figure 4-2 to Figure 4-6 show the mouse in the smart cage while testing the food removal unit. The mouse reaction can be seen while the gate of the food container is opening and closing. Apparently, the mouse does not fear from the gate's movement and stays close to the gate while it is moving.

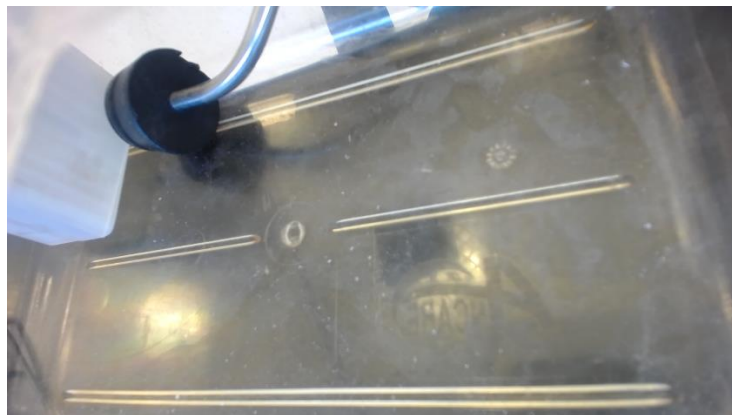


Figure 4-1- a captured image from the cage area by Logitech web camera seated on the tray. This frame shows the area covered with the Logitech camera.



Figure 4-2- Captured frame from a recorded video by Logitech C930 webcam located on the tray.



Figure 4-3- Captured frame from a recorded video by Logitech C930 webcam located on the tray. As it can be seen there is a blurring on the image due to the reflective surface of PLC covering the camera spot.

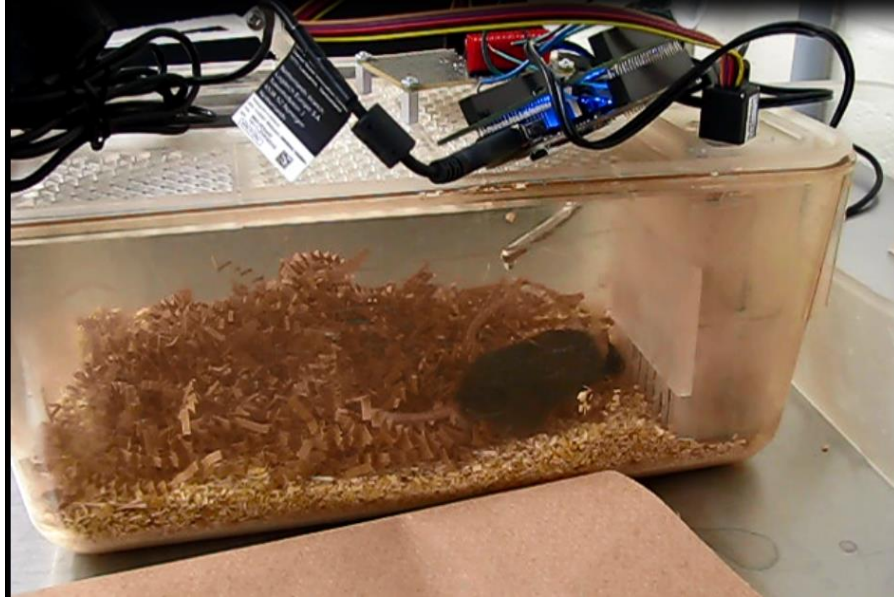


Figure 4-4- A captured image using an external camera while testing the food removal unit in the animal facility at the University of Manitoba. At this moment the gate of the food container is opening. The lid has been removed while testing to have access to the camera located on the tray to change its angle.

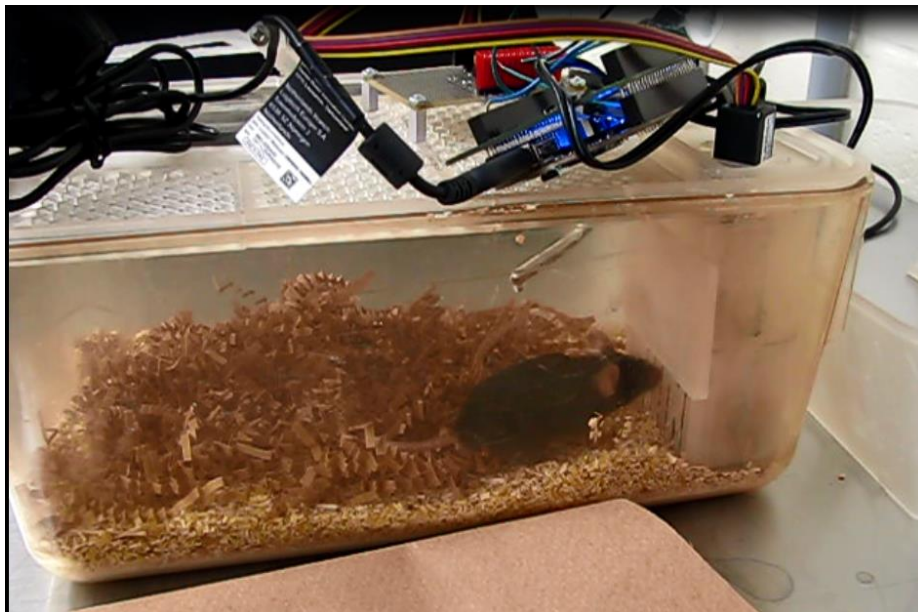


Figure 4-5- A captured image using an external camera while testing the food removal unit in the animal facility at the University of Manitoba. At this moment the gate of the food container is opening. The lid has been removed while testing to have access to the camera located on the tray to change its angle.



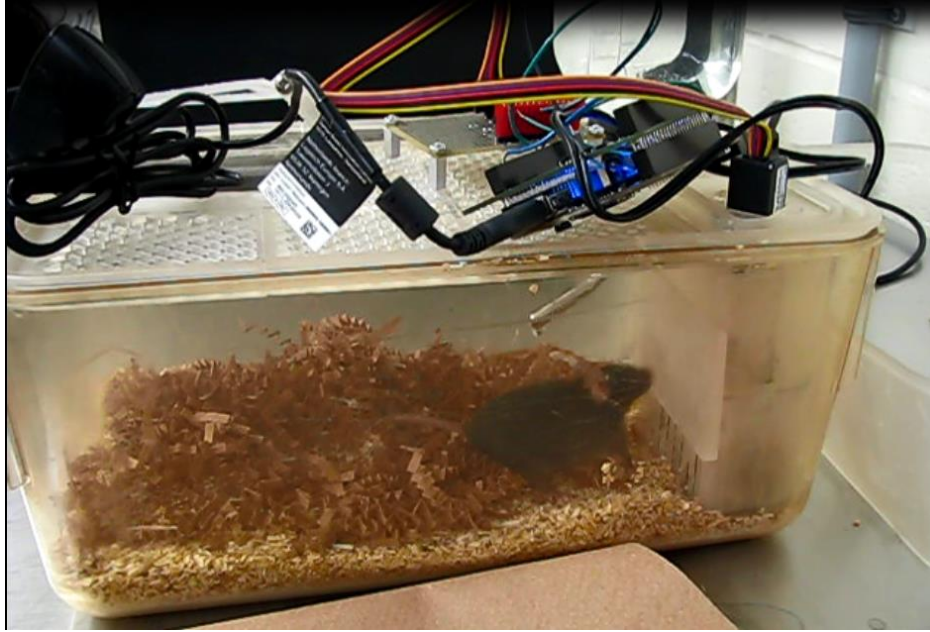


Figure 4-6- A captured image using an external camera while testing the food removal unit in the animal facility at the University of Manitoba. At this moment the gate of the food container is closing. The lid has been removed while testing to have access to the camera located on the tray to change its angle.

#### **4.4 Motion tracking diagrams**

One of the novelties of the smart cage is its motion detection and tracking option. The programming and methodology of it has been described in detail in Chapter 3. In this section we will review the results of applying this algorithm to the recorded videos using the Reolink C1pro and Logitech C930e web camera.

To check the performance of this option with the Reolink C1 pro camera, videos of a mouse have been recorded in a cage while a Reolink C1 pro camera was placed in front of the cage. The recording process lasted two consecutive days and one video file was recorded every 15 minutes. Figure 4-7 and Figure 4-8 show the detected motions of the mouse during the night along the x and y axis. In this 15 minute period, the mouse is asleep. The detected movements are associated with the small movements of the mouse during its sleep and the corresponding movements of the shredded papers covering its body. To verify whether the detected movements are true or false,

the captured frames during the times which the motion diagrams show the movements have been checked. Figure 4-9 and Figure 4-10 show the corresponding frames before and after the detected movement which was highlighted in previous diagrams. As a conclusion, while the light level and intensity is steady and constant in the background, the detected motions are true. However, the amplitude of the detected motions which is expressed by the pixels' value is not quite accurate. This inaccuracy originates from the implemented motion detection algorithm. The detected motion is in fact the result of subtraction the current frame from the background frame after adding a Gaussian filter. If the result of this subtraction is greater than a defined number of pixels, it will be classified as a motion. The returned value from the motion detection algorithm is the (x, y) of the center of mass of the area that has been varied between the two frames. Clearly, we are not tracking the same point during the recording time to calculate the magnitude of the motion. However, our goal which was detecting the motions of the mouse is achieved by applying this method.

Figure 4-11 and Figure 4-12 show the motion diagrams of the mouse during daylight. As the diagram shows, the mouse is awake due to its high frequency of activity. Figure 4-13 and Figure 4-14 are the corresponding frames to the highlighted movement on the motion diagrams.

Figure 4-16 and Figure 4-17 illustrate the motion summaries of the tested mouse during the intervals of two and four hours. To generate these graphs, the relative motion of the mouse was considered instead of the absolute one. Next, the calculated relative motions have been converted to the binary output. The binary output in this case means if there was a motion the result would be one and if there was no detected movement the result would be zero. Then, the accumulative binary motion was calculated and drawn in a graph to illustrate how active the mouse has been during the time interval.

To evaluate the performance of the motion detection program with the Logitech C930e web camera, another test has been done. During this test, the animal was stayed inside of the smart cage for a duration of 1 hour and videos with 2 minutes duration were recorded. Each of these videos were analyzed using the motion detection program simultaneously and the output was recorded as motion diagram, Figure 4-15. As Figure 4-15 shows the motion diagram of the mouse when it is monitored by the Logitech C930 e web camera is smoother due to lower frame rate of the camera.



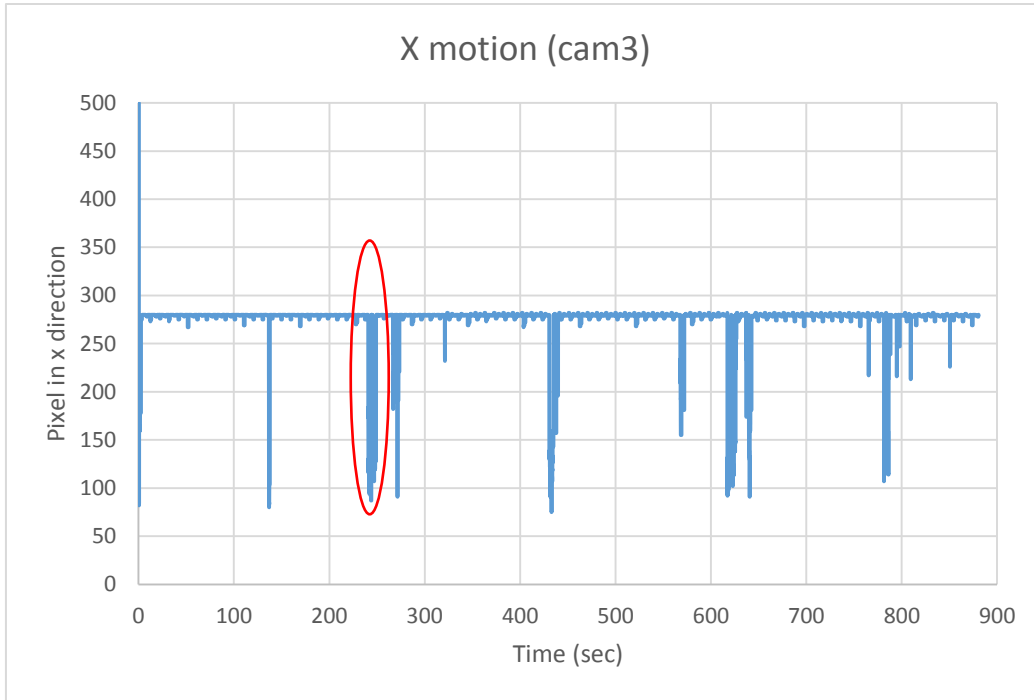


Figure 4-7- Motion diagram of a mouse in x direction during the night. The length of the video is 15 minutes.

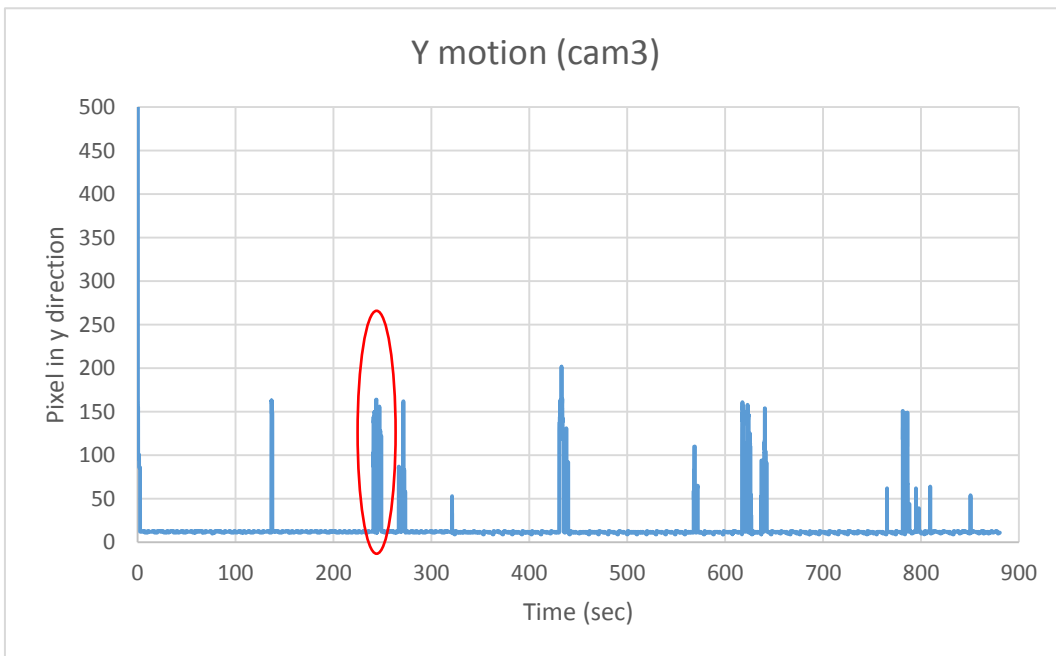


Figure 4-8- Motion diagram of a mouse in y direction during the night. The length of the video is 15 minutes.



Figure 4-9- A captured frame of the recorded video which shows the state of animal before the detected motion. This frame was captured during the night in night vision mode. The red circle shows the area where the motion will happen.



Figure 4-10- A captured frame of the recorded video which shows the state of animal after the detected motion. This frame was captured during the night in night vision mode. The red circle shows the area where the motion happened.

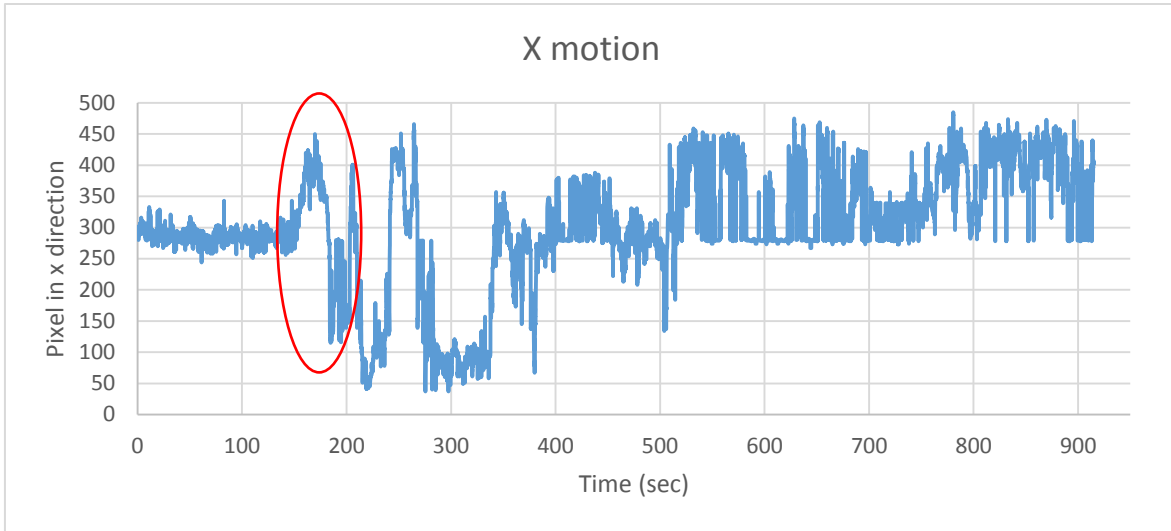


Figure 4-11- Motion diagram of a mouse in x direction during the day. The length of the video is 15 minutes.

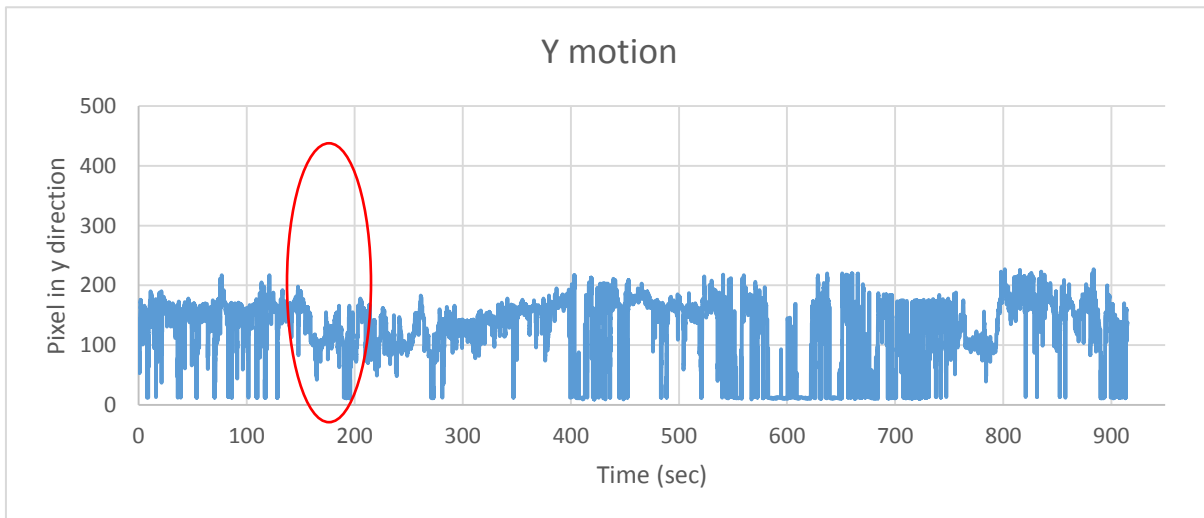


Figure 4-12- Motion diagram of a mouse in y direction during the day. The length of the video is 15 minutes.



Figure 4-13- A captured frame of the recorded video which shows the state of animal before the detected motion.



Figure 4-14- A captured frame of the recorded video which shows the state of animal after the detected motion.

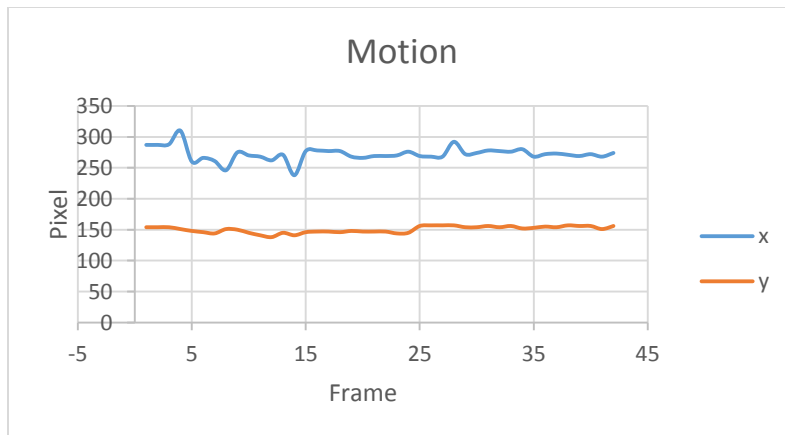


Figure 4-15- Motion diagram of a mouse in x and y direction during the day. The length of the video is 2 minutes. This video is recorded by Logitech C930 camera. The motion detection program ran by BBBW.

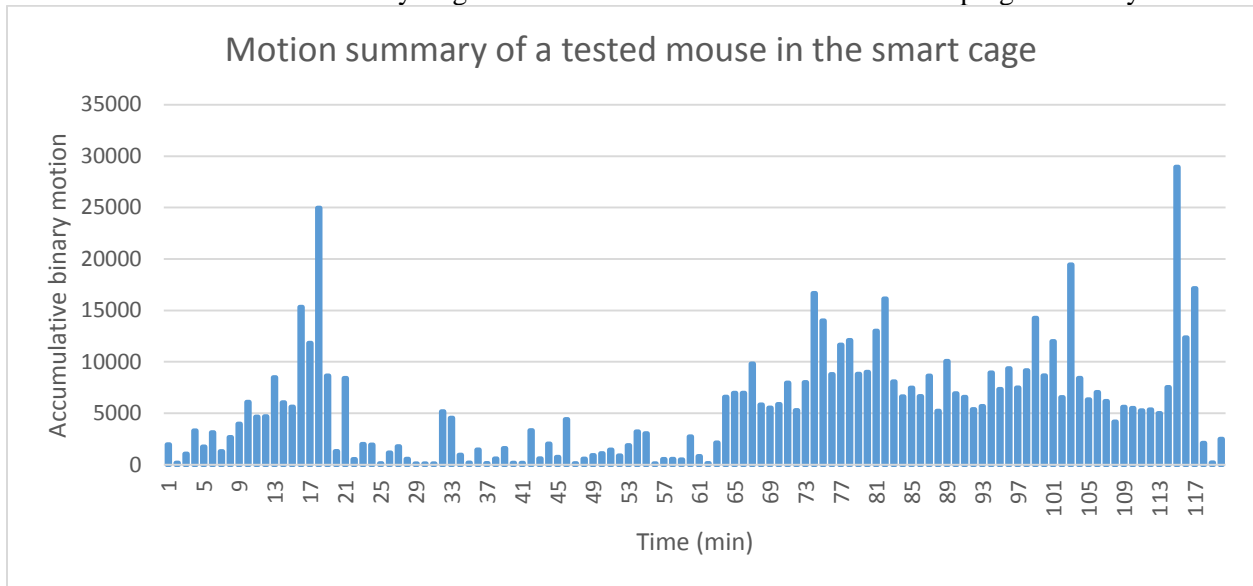


Figure 4-16- Motion summary of a tested mouse during 2 hours in daylight. The recording has been started at 11:52 AM on October 18th in the animal facility at the University of Manitoba.

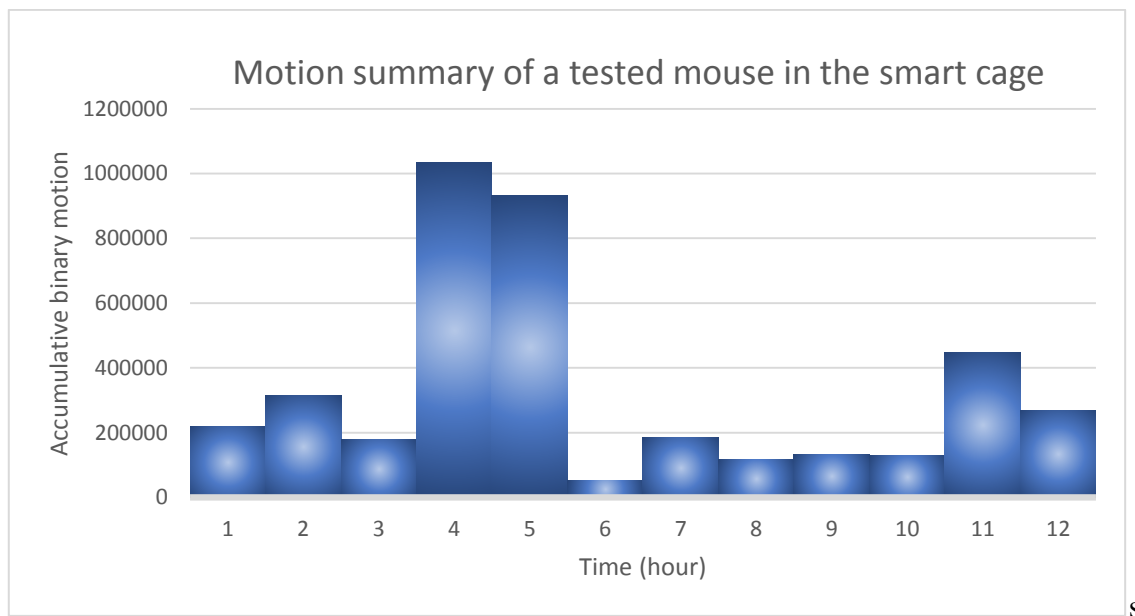


Figure 4-17- Motion summary of a tested mouse during 12 hours in daylight with 1 hour interval. The recording has been started at 11:52 AM on October 18th in the animal facility at the University of Manitoba and continued for 24 hours.

## Chapter 5

### 5. Conclusion and future works

Positron emission tomography (PET) is a nuclear medicine imaging technique that allows quantitative evaluation of positron emitting radioactive tracers injected into a subject. In both clinical and research settings, the most commonly used radiotracer for PET imaging is the glucose analog [18F]fluorodeoxyglucose (FDG). The central strength and challenge in PET imaging is that the resulting image is of the biodistribution of the radioactively labelled tracer, rather than simply an image of anatomy. This means that biological factors can greatly influence both the appearance and quantification of the PET image, especially for FDG since it is a marker of glucose metabolism. These effective factors include fasting, anesthesia and warming the animal's body in animal PET imaging. In addition, the animals' health status must be monitored after imaging. A significant cost in routine small animal PET imaging is the labour associated with the imaging procedures. These animal centre labour costs can be reduced through use of automation and remote monitoring.

In consideration of the above points, we saw an unmet need for a better approach to animal preparation and monitoring post-procedure and developed a 'Smart Cage' that automates feeding and allows remote monitoring of the animal before and after the imaging. Furthermore, the requirements of follow up monitoring of animals are not unique to imaging procedures and it can be applied after surgical or other procedures. By taking advantage of an 'internet of things' design, treating the cage as a programmable network appliance, we are able to reduce the amount of time the animal imaging technician must spend with each subject.

## **5.1 Summary and conclusion**

As described earlier, a smart cage has been developed and constructed to automate animal handling before PET imaging and the follow up monitoring. The designed smart cage contains automated food removal unit and remote monitoring module.

The result of testing different modules of the smart cage appeared promising. As explained in Chapter 4, the animal showed no symptoms of short term distress while stayed in the smart cage. The reaction of animal to a cyclic opening and closing the gate of food container was observed for one hour period in animal facility at the University of Manitoba.

The remote monitoring module of the smart cage has been tested in the animal facility at the University of Manitoba. During the first test, the day camera installed on the cage has been tested for a period of one hour. The output of this test includes 60 frames (1 frame per minute) and one hour video with 1 frame per second. In addition, the night vision camera has been tested for 48 hours in the animal facility at the University of Manitoba.

The utilization of the designed smart cage leads to reduced labor cost of animal handling before PET imaging and its follow up monitoring.

## **5.2 Future works**

Beyond the discussed benefits of utilizing the smart cage, there are many possible ways to extend the capability of the smart cage. Following are the suggested ways to improve the capabilities of this device:

### **5.2.1 Capability and reproducibility test**

As mentioned earlier, the smart cage has been tested for a short period of time in the animal facility at the University of Manitoba. A long term testing is essential to assess the cage effects on animal distress level and comfort.

In addition, to evaluate the effect of the smart cage's utilization on the reproducibility of the PET images a reproducibility test can be designed and conducted.

### **5.2.2 Using Cloud system instead of host PC**

Using a host PC results in some limitations. It has a limited memory capacity. If the user wants to change the setting of the program must access the host PC directly. If several smart cages connect to the host PC, it should be able to run the motion detection program on all of them which needs a powerful processor. By replacing cloud system instead of host PC, we can take advantage of unlimited memory and powerful processing capacity. In the way, there is no need to host PC that results in less complication for cable connections and less occupied space in the room. Using this method, the router will be replace with a gateway. Each smart cage communicates bidirectly with the cloud directly using the gateway.

### **5.2.3 Controllable heating module**

Another helpful module that can be added to the smart cage is heating module. According to the research studies by several groups, heating the animal affects the uptake level of  $^{18}\text{F}$ -FDG in tumors [23]. To take advantage of this fact, a heating pad can be placed at the bottom of the cage and be controlled to maintain a suitable and steady environment temperature for the animal.



#### **5.2.4 Revising the frame of the smart cage**

In next generations of the smart cage, the design of the frame can be revised so that all the components are kept outside of the smart cage in a control unit except the linear actuator. By placing the camera in the control unit in a suitable distance from the cage, this goal is doable.

## References

- [1] S. R. Cherry, J. A. Sorenson and M. E. Phelps, "Positron Emission Tomography," in *Physics in Nuclear Medicine*, Elsevier Inc., 2012, pp. 307-343.
- [2] M. E. Phelps, "PET: the merging of biology and imaging into molecular imaging," *The Journal of Nuclear Medicine*, pp. 661-681, 2000.
- [3] A. K. Buck, K. Herrmann, T. Stargardt, T. Dechow, B. J. Krause and J. Schreyogg, "Economic Evaluation of PET and PET/CT in Oncology: Evidence and Methodologic Approaches," *Journal of nuclear medicine*, vol. 51, pp. 401 -412, 2010.
- [4] R. Boellaard, "Standards for PET Image Acquisition and Quantitative Data Analysis," *Journal of nuclear medicine*, vol. 50, pp. 11S - 20S, 2009.
- [5] G. B. Saha, Basics of PET Imaging, Springer International Publishing, 2016.
- [6] J. J. Vaquero and P. Kinahan, "Positron Emission Tomography: Current Challenges and Opportunities for Technological Advances in Clinical and Preclinical Imaging Systems," *Annual Review of Biomedical Engineering*, vol. 17, pp. 385-414, 2017.
- [7] S. R. Cherry, J. A. Sorenson and M. E. Phelps, "Positron Emission Tomography," in *Physics in Nuclear Medicine*, Philadelphia, Elsevier Health Sciences, 2012, pp. 307-343.
- [8] J. Pacak, Z. Tocik and M. Cerny, "Synthesis of 2-deoxy-2-fluoro-D-glucose," *Journal of the Chemical Society D: Chemical Communications*, no. 2, pp. 77-77, 1969.
- [9] P. Lindholm , H. Minn, S. Leskinen-Kallio, J. Bergman , U. Ruotsalainen and H. Joensuu, "Influence of the blood glucose concentration on FDG uptake in cancer--a PET study," *Journal of Nuclear Medicine*, vol. 34, pp. 1-6, 1993.
- [10] "Fludeoxyglucose F 18 (Systemic)," [Online]. Available: <https://www.drugs.com/mmx/fludeoxyglucose-f-18.html>.
- [11] petchemist, "PET Chemist," [Online]. Available: <https://petchemist.wordpress.com/>.
- [12] D. S. Surasi, P. Bhambhvani, J. A. Baldwin, S. E. Almodovar and J. P. O'Malley , "18F-FDG PET and PET/CT Patient Preparation: A Review of the Literature," *Journal of Nuclear Medicine Technology*, vol. 42, pp. 5-13, 2014.

- [13] P. E. Kinahan and J. W. Fletcher, "PET/CT Standardized Uptake Values (SUVs) in Clinical Practice and Assessing Response to Therapy," *Seminars in Ultrasound, CT and MRI*, vol. 31, no. 6, pp. 496-505, 2010.
- [14] T. Torizuka, A. C. Clavo and R. L. Wahl, "Effect of hyperglycemia on in vitro tumor uptake of tritiated FDG, thymidine, L-methionine and L-leucine," *Journal of Nuclear Medicine*, pp. 382-386, 1997.
- [15] R. L. Wahl, C. A. Henry and S. P. Ethier, "Serum glucose: effects on tumor and normal tissue accumulation of 2-[F-18]-fluoro-2-deoxy-D-glucose in rodents with mammary carcinoma," *Radiology*, vol. 183, no. 3, pp. 643-647, 1992.
- [16] S. S. B. J. W. K. Büsing KA, "Impact of blood glucose, diabetes, insulin, and obesity on standardized uptake values in tumors and healthy organs on 18 F-FDG PET/CT," *Nucl Med Biol*, vol. 40, no. 2, pp. 206-213, 2013.
- [17] D. S. B. J. P. A. Keramida G, "Quantification of tumour 18 F-FDG uptake: Normalise to blood glucose or scale to liver uptake?," *European Radiology*, vol. 25, p. 2701–2708, 2015.
- [18] W. K. W. S. P. A. N. B. K. C. e. a. Viglianti BL, "Effect of hyperglycemia on brain and liver 18F-FDG standardized uptake value (FDG SUV) measured by quantitative positron emission tomography (PET) imaging," *Biomedicine & Pharmacotherapy*, vol. 88, pp. 1038-1045, 2017.
- [19] M. K. A. Y. Claeys J, "Normoglycemic plasma glucose levels affect F-18 FDG uptake in the brain," *Annals of Nuclear Medicine*, vol. 24, p. 501–505, 2010.
- [20] C. Sprinz, S. Altmayer, M. Zanon, G. Watte, K. Irion, E. Marchiori and B. Hochegger , "Effects of blood glucose level on 18F-FDG uptake for PET/CT in normal organs: A systematic review," *PLOS One*, 2018.
- [21] R. E. C. M. J. G. e. a. Dominique Delbeke, "Procedure Guideline for Tumor Imaging with 18F-FDG PET/CT 1.0," *Journal of nuclear medicine*, vol. 47, no. 5, pp. 885-895, 2006.
- [22] J. P. B. S. D. K. E. V. N. B. a. S. V. Christian Vanhove, "Accurate molecular imaging of small animals taking into account animal models, handling, anaesthesia, quality control and imaging system performance," *European Journal of Nuclear Medicine and Molecular Imaging physics*, vol. 2, no. 31, pp. 1 - 25, 2015.
- [23] B. J. Fueger, J. Czernin, I. Hildebradt, C. Tran, B. S. Halpern, D. Stout and et al, "Impact of animal handling on the results of 18F-FDG PET studies in mice," *Journal of nuclear*

*medicine*, vol. 47, pp. 999 -1006, 2006.

- [24] J. A. R. J. C. E. C. J. E. v. L. R. L. F. B. Antonio Aliaga, "A Small Animal Positron Emission Tomography Study of the Effect of Chemotherapy and Hormonal Therapy on the Uptake of 2-Deoxy-2-[F-18]fluoro-D-glucose in Murine Models of Breast Cancer," *Molecular Imaging Biology*, no. 9, pp. 144-150, 2007.
- [25] O. J. K. J. D. P. Jen-Chieh Tseng, "Preclinical In Vivo Imaging," PerkinElmer, Waltham, 2017.
- [26] O. team, "OpenCV," 2019. [Online]. Available: <https://opencv.org/>.
- [27] R. B. P. KaewTraKulPong, "An Improved Adaptive Background Mixture Model for Realtime Tracking with Shadow Detection," in *2nd European Workshop on Advanced Video Based Surveillance Systems*, 2001.
- [28] Z. Zivkovic, "Improved Adaptive Gaussian Mixture Model for Background Subtraction," in *17th International Conference on Pattern Recognition*, Cambridge, 2004.
- [29] F. v. d. H. Zoran Zivkovic, "Efficient Adaptive Density Estimation per Image Pixel for the Task of Background Subtraction," *Pattern Recognition Letters*, vol. 27, no. 7, pp. 773-780, 2006.
- [30] A. M. K. G. Andrew B. Godbehere, "Visual Tracking of Human Visitors under Variable-Lighting Conditions for a Responsive Audio Art Installation," in *American Control Conference (ACC)*, Montreal, 2012.
- [31] S. S. a. I. W. Linda Rosencrance, "Internet of things agenda," TechTarget, 2019. [Online]. Available: <https://internetofthingsagenda.techtarget.com/definition/Internet-of-Things-IoT>. [Accessed 2018].
- [32] X. Benhai, Y. Liang, P. Xiaohua and Y. Zhengang, "Review on application of Internet of Things technology in animal husbandry in China," *Transactions of the Chinese Society of Agricultural Engineering*, vol. 31, pp. 237-246, 2015.
- [33] D. S. S. L. A. B. N. M. Mohamed Zaki and Andy Neely, "Internet of Animal Health Things (IoAHT)," Cambridge Service Alliance.
- [34] Beagleboard, "beagleboard," the BeagleBoard.org Foundation, [Online]. Available: [beagleboard.org](http://beagleboard.org).
- [35] "Digikey," [Online]. Available: <https://forum.digikey.com/t/beaglebone-black-wireless-the->

octavo-osd335x/384.

- [36] "Actuonix," [Online]. Available: <https://www.actuonix.com/L12-P-Micro-Linear-Actuator-with-Position-Feedback-p/112-p.htm>.
- [37] [Online]. Available: [https://support.logitech.com/en\\_us/product/webcam-c930e-business/specs](https://support.logitech.com/en_us/product/webcam-c930e-business/specs).
- [38] [Online]. Available: [https://reolink.com/product/c1-pro/?gclid=CjwKCAjwuO3cBRAyEiwAzOxKsnm4HL-vmgeMR2-gL9g\\_V0R2IbBo83b8zQc3MWCP-l2D5DgP-g0FmRoCNVcQAvD\\_BwE](https://reolink.com/product/c1-pro/?gclid=CjwKCAjwuO3cBRAyEiwAzOxKsnm4HL-vmgeMR2-gL9g_V0R2IbBo83b8zQc3MWCP-l2D5DgP-g0FmRoCNVcQAvD_BwE).
- [39] "Capemgr," [Online]. Available: <https://elinux.org/Capemgr>.
- [40] "The Lightweight Qt Desktop Environment," [Online]. Available: <https://lxqt.org/>.
- [41] "Introduction to At-Spi2 Core," 2019. [Online]. Available: <http://www.linuxfromscratch.org/blfs/view/svn/x/at-spi2-core.html>.
- [42] "LabWindows/CVI," National Instruments, 2019. [Online]. Available: <https://www.ni.com/lwcvl/>.
- [43] "Introducing WinSCP," WinSCP.net , 2019. [Online]. Available: <http://winscp-static-746341.c.cdn77.org/eng/docs/introduction>.
- [44] A. Rosebrock, "Basic motion detection and tracking with Python and OpenCV," pyimagesearch, May 2015. [Online]. Available: <https://www.pyimagesearch.com/2015/05/25/basic-motion-detection-and-tracking-with-python-and-opencv/>.
- [45] N. B. Mitchell, "A simple method for hardware and software evaluation," *Applied Ergonomic*, vol. 23, no. 4, pp. 277-280 , 1992.
- [46] P. INTERNATIONAL, "ABS material datasheet," PLASTICS INTERNATIONAL.
- [47] N. R. C. Committee on Recognition and Alleviation of Distress in Laboratory Animals, *Recognition and Alleviation of Distress in Laboratory Animals*, Washington D.C.: National Academy of Sciences, 2008.
- [48] A. Granov, L. Tiutin and T. Schwarz, "The Physical Basis of Positron Emission Tomography," in *Positron Emission Tomography*, Berlin, Springer, 2011, pp. 3-24.

- [49] M. Dandekar, J. R. Tseng and S. Gambhir, "Reproducibility of 18F-FDG microPET Studies in Mouse Tumor Xenografts," *Journal of nuclear medicine*, vol. 48, pp. 602 -607, 2007.
- [50] A. L. Goertzen and H. Zaidi, "Dual-Modality Preclinical PET/CT Instrumentation," in *Molecular Imaging of Small Animals: Instrumentation and Applications*, New York, Springer, 2014, pp. 367 - 386.
- [51] A. L. Goertzen, G. Stortz, J. D. Thiessen, D. Bishop, M. S. Khan, P. Kozlowski and et al, "First Results from a High-Resolution Small Animal SiPM PET Insert for PET/MR Imaging at 7T," *IEEE Transactions on Nuclear Science*, vol. 63, pp. 2424 - 2433, 2016.
- [52] A. L. Goertzen, Q. Bao, M. Bergeron, E. Blankemeyer, S. Blinder, M. Canadas and et al, "NEMA NU 4-2008 comparison of preclinical PET imaging systems," *Journal of nuclear medicine*, vol. 53, pp. 1300 -9, 2012.
- [53] D. A. Mankoff and J. R. Bellon, "Positron-emission tomographic imaging of cancer: Glucose metabolism and beyond," *Seminars in Radiation Oncology*, vol. 11, pp. 16 -27, 2001.
- [54] L. Mosconi, W. H. Tsui, K. Herholz, A. Pupi, A. Drzezga, G. Lucignani and et al, "Multicenter Standardized 18F-FDG PET Diagnosis of Mild Cognitive Impairment, Alzheimer's Disease, and Other Dementias," *Journal of nuclear medicine*, vol. 49, pp. 390 - 398, 2008.
- [55] Y. C. Tai and R. Laforest, "Instrumentation aspects of animal pet," *Annual Review of Biomedical Engineering*, vol. 7, pp. 255 -285, 2005.
- [56] J. R. Tseng, M. Dandekar, M. Subbarayan, Z. Cheng, J. M. Park, S. Louie and et al, "Reproducibility of 3'-Deoxy-3'-18F-Fluorothymidine MicroPET Studies in Tumor Xenografts in Mice," *Journal of nuclear medicine*, vol. 46, pp. 1851 - 1857, 2005.
- [57] T. G. Turkington, "PET Imaging Basics," in *Clinical PET-CT in Radiology*, New York, Springer, 2011, pp. 21-28.
- [58] Formlabs, "Clear Photopolymer Resin for Form 1+ and Form 2 FLGPCL03 MATERIAL PROPERTIES," Formlabs, 2016.
- [59] IPEX, ABS CHEMICAL RESISTANCE GUIDE, Mississauga: IPEX, 2009.
- [60] M. Jackson, . S. Crouch and R. Baxter, "Software Evaluation: Criteria-based Assessment," Software sustainability Institute, 2011.